AFRL-AFOSR-VA-TR-2018-0369

Isolated Soft-X-ray Attosecond Pulse Generation Using Synthesized Strong-Field Mid-IR Pulses

Kyung-Han Hong
MASSACHUSETTS INSTITUTE OF TECHNOLOGY

03/06/2018
Final Report

Air Force Research Laboratory
AF Office Of Scientific Research (AFOSR)/ RTB1
Arlington, Virginia 22203
Air Force Materiel Command

REPORT DOCUMENTATION PAGE

Form Approved
OMB No. 0704-0188

1. REPORT DATE *(DD-MM-YYYY)*	**2. REPORT TYPE**	***3.* DATES COVERED** *(From - To)*
26-09-2018	FinalPerformance	01 Sep 2014 to 30 Nov 2017

4. TITLE AND SUBTITLE
Isolated Soft-X-ray Attosecond Pulse Generation Using Synthesized Strong-Field Mid-IR Pulses

5a. CONTRACT NUMBER

5b. GRANT NUMBER
FA9550-14-1-0255

5c. PROGRAM ELEMENT NUMBER
61102F

6. AUTHOR(S)
Kyung-Han Hong, FranzKaertner

5d. PROJECT NUMBER

5e. TASK NUMBER

5f. WORK UNIT NUMBER

7. PERFORMING ORGANIZATION NAME(S) AND ADDRESS(ES)
MASSACHUSETTS INSTITUTE OF TECHNOLOGY
77 MASSACHUSETTS AVE
CAMBRIDGE, MA 02139-4301 US

8. PERFORMING ORGANIZATION REPORT NUMBER

9. SPONSORING/MONITORING AGENCY NAME(S) AND ADDRESS(ES)
AF Office of Scientific Research
875 N. Randolph St. Room 3112
Arlington, VA 22203

10. SPONSOR/MONITOR'S ACRONYM(S)
AFRL/AFOSR RTB1

11. SPONSOR/MONITOR'S REPORT NUMBER(S)
AFRL-AFOSR-VA-TR-2018-0369

12. DISTRIBUTION/AVAILABILITY STATEMENT
A DISTRIBUTION UNLIMITED: PB Public Release

13. SUPPLEMENTARY NOTES

14. ABSTRACT
he MIT-KSU 'Isolated Attosecond Pulse Generation Using Synthesized Mid-IR Pulses' program enabled not only to develop novel few-cycle and sub-cycle mid-IR laser sources based on OPA, OPCPA, and pulse synthesis but also to study strong-field physics and extreme nonlinear optics driven by mid-IR laser pulses in the wavelength range of 2-10 um. Specifically, we developed a long-term stable, multi-mJ, kHz, 26 fs, 2.1 um OPCPA as a primary driving source for this project. Using this unique source, we experimentally demonstrated 1) water-window soft X-ray HHG up to 450 eV, 2) sub-cycle control of soft X-ray yields from two-color (w+3w) driven HHG, 3) multi-octave-spanning mid-IR laser filamentation and self-compression in solids 4) kHz femtosecond laser filamentation in ambient air, for the first time, 4) sub-cycle pulse synthesis from an OPA in the wavelength range of 2.5-10 um, 5) near-continuous harmonic spectra from solid-state HHG in silicon as a signature of isolated harmonic emission, for the first time. Our theoretical studies uncover how to improve the characteristics of high harmonics in different spectral regions from both the single-atom and macroscopic aspects, by optimizing the macroscopic parameters and the multi-color laser waveforms, and by increasing the gas pressure in a high-ionization medium. Through the balanced efforts on experiment and theory, we have made significant advancements on novel laser source technology and

15. SUBJECT TERMS
attosecond, strong-field, Mid-IR, soft x-ray

16. SECURITY CLASSIFICATION OF:			**17. LIMITATION OF ABSTRACT**	**18. NUMBER OF**	**19a. NAME OF RESPONSIBLE PERSON**
a. REPORT	**b. ABSTRACT**	**c. THIS PAGE**			PARRA, ENRIQUE

Standard Form 298 (Rev. 8/98)
Prescribed by ANSI Std. Z39.18

Unclassified	Unclassified	Unclassified	UU	**PAGES**	**19b. TELEPHONE NUMBER** *(Include area code)* 703-696-8571

REPORT ON AFOSR CONTRACT# FA9550-14-1-0255
To: technicalreports@afosr.af.mil
Subject: Final Progress Statement to Dr. Enrique Parra

TITLE: ISOLATED ATTOSECOND PULSE GENERATION USING SYNTHESIZED MID-IR PULSES

Sept. 2014 – Nov. 2017, Final Report

PI: Kyung-Han Hong

Massachusetts Institute of Technology (MIT),
Research Laboratory of Electronics (RLE)
Rm: 36-389, 77 Massachusetts Ave., Cambridge, MA 02139
Tel: 617 452-3616, Fax: 617 253-9611, email: kyunghan@mit.edu

Co-PI
Franz X. Kärtner, RLE, MIT
Chii-Dong Lin, Dept. of Physics, Kansas State University

ISOLATED ATTOSECOND PULSE GENERATION USING SYNTHESIZED MID-IR PULSES

I. Goals of project and summary of results achieved:

1. Original goals of project

1) To generate and characterize isolated soft X-ray high-harmonic attosecond pulses (>200 eV) using synthesized mid-infrared (mid-IR) laser pulses
2) To demonstrate the efficiency enhancement and the coherent control of electron wavepackets (EWPs) during high-harmonic generation (HHG)
3) To perform precision soft X-ray high-harmonic spectroscopy (HHS) of atoms and molecules with the help of the accurate calculation of macroscopic EWPs and Quantitative Rescattering (QRS) theory

2. Updated goals of project

1) To generate and characterize attosecond soft X-ray HHG up to water-window range (280-540 eV) using mid-IR laser pulses
2) To demonstrate the efficiency enhancement and sub-cycle control of HHG up to the soft X-ray range
3) Theoretical study of optimal HHG and isolated attosecond pulse generation by adjusting macroscopic conditions
4) Theoretical study of waveform synthesizer for enhancing the yields of water-window high harmonics
5) To demonstrate mid-IR laser filamentation in ambient air at kHz repetition rate
6) To demonstrate sub-cycle waveform synthesis in the mid-IR range
7) To study solid-state HHG using synthesized mid-IR pulses for isolated harmonic emission toward petahertz electronics in solids

3. Summary of program accomplishments:

3.1 Soft X-ray HHG in gases using mid-IR laser pulses (Year 1)

- Improvement of long-term stability of multi-mJ, kHz, 2.1 μm optical parametric chirped pulse amplifier (OPCPA) using a hybrid Yb-doped pump laser
- Water-window soft X-ray HHG in Ne up to 450 eV using 2.1 μm driver pulses with a photon flux of ~10^6 photon/second over 1% bandwidth
- Water-window soft X-ray attosecond pulse train confirmed by HHG simulations

3.2 Sub-cycle control of soft X-ray HHG using synthesized mid-IR waveforms (Years 2-3)

- Development of a dichroic Michaelson interferometer for ω (2.1 μm) and 3ω (700 nm) mixing
- Demonstration of efficiency enhancement of two-color (ω+3ω) driven HHG by one order of magnitude

- Control of HHG efficiency with sub-cycle precision and study of pressure dependence
- Comparison with HHG simulations based on 3D propagation and QRS theory
- Theoretical study of optimal high harmonic generation by adjusting macroscopic conditions
- Theoretical study of waveform synthesizer for enhancing the yields of water-window HHG

3.3 Mid-IR laser filamentation in solids and air (Years 1-2)
- Multi-octave-spanning mid-IR laser filamentation in solid materials with different dispersion characteristics
- First demonstration of mid-IR laser filamentation in ambient air at a high repetition rate (1 kHz)

3.4 Mid-IR sub-cycle pulse synthesis and solid-state HHG (Years 2-3)
- First demonstration of sub-cycle mid-IR pulse synthesis from an optical parametric amplifier (OPA) covering 2.5-10 μm
- Study of solid-state HHG in various solids (silicon, NiO_2, MgO, and diamond)
- Continuous harmonic emission with sub-cycle driver, indicating isolated harmonic emission
- Demonstration of a femtosecond ~8 μm source based on a 2.1 μm pumped intrapulse difference-frequency generation (DFG) for the first time

II. Detailed Description of Systems Constructed and Results Achieved

1. Soft X-ray HHG in gases using mid-IR laser pulses

Mid-IR drivers are ideal for extending the cutoff of HHG in gases into the soft X-ray water-window and even keV regime [Takahashi08, Popmintchev11]. In this project, we first finished the upgrade of existing multi-mJ kHz 2.1 μm OPCPA at MIT [Hong14] and then demonstrated the HHG cutoff extension to water-window range [Stein16] using this driving source. HHG simulations confirmed the attosecond soft X-ray pulse train in the water-window region.

1.1 Long-term stable, kHz, 2.1 μm OPCPA pumped by a hybrid Yb-doped pump laser

As an upgrade of previously developed all-cryogenic Yb:YAG pump laser [Hong14], we developed a high-energy, kHz, picosecond pump laser based on a hybrid Yb-doped chirped-pulse amplifier. By combining a Yb:KYW regenerative amplifier (RGA) and cryogenic Yb:YAG multipass amplifiers (MPAs), we generated up to 70 mJ of energy at 1030 nm for pumping our OPCPA. The Yb:KYW amplifier minimizes the gain narrowing that has been a main issue with the previous cryogenic Yb:YAG RGA and enables to avoid accumulation of nonlinear phase in the chirped-pulse amplification (CPA) scheme. With the installation of a beam pointing stabilizer for the pulse compressor of this hybrid laser and an automatic liquid nitrogen refilling system for continuous cooling Yb:YAG crystals we were able to achieve a long-term stability over 8 hours of continuous operation, which is long enough for HHG experiments with delay scans.

Figure 1 shows the schematic diagram of the sub-10 ps, hybrid Yb-doped CPA laser for pumping our 2.1 μm OPCPA. It is composed of a seed oscillator, three Yb-doped fiber pre-amplifiers, a stretcher, a room-temperature Yb:KYW RGA, two cryogenic Yb:YAG MPAs, and a pulse compressor. The basic CPA architecture follows our previous works [Hong10, Hong11] and is optimized for pumping ultrabroadband OPCPAs. An octave-spanning Ti:sapphire oscillator (Octavius-85M, IdestaQE/Thorlabs) generates few-cycle femtosecond laser pulses with an average

power of ~200 mW at 85 MHz repetition rate, which are used to seed the OPCPA and pump lasers. Approximately 90% of the light in the spectral range from 1010 nm to 1060 nm, corresponding to ~2 mW of average power, is extracted and amplified in a single-mode (SM) Yb-doped fiber amplifier (YDFA), as indicated as YDFA 0 in Fig. 1. We then further narrow the spectral range to a ~4 nm bandwidth centered at ~1030 nm using a bandpass filter, and amplify in YDFA 1 indicated in Fig. 1 to precompensate for the losses in the stretcher. The compact stretcher consists of a pair of chirped volume Bragg gratings (CVBGs) with a chirp rate of ~100 ps/nm per bounce over a 2-nm operation bandwidth (for each CVBG). The total footprint of the stretcher is 20 cm by 15 cm. After 8 bounces off the CVBGs (Ondax Inc.), giving a total chirp rate of ~800 ps/nm, we obtain positively-chirped pulses with a temporal width of ~680 ps in full-width at half-maximum (FWHM), determined by the measured spectrum of the stretched pulses. The reflection loss in the CVBG stretcher is compensated by YDFA 2 in Fig. 1, and a pulse energy of ~0.5 nJ at 85 MHz is delivered to the input of RGA.

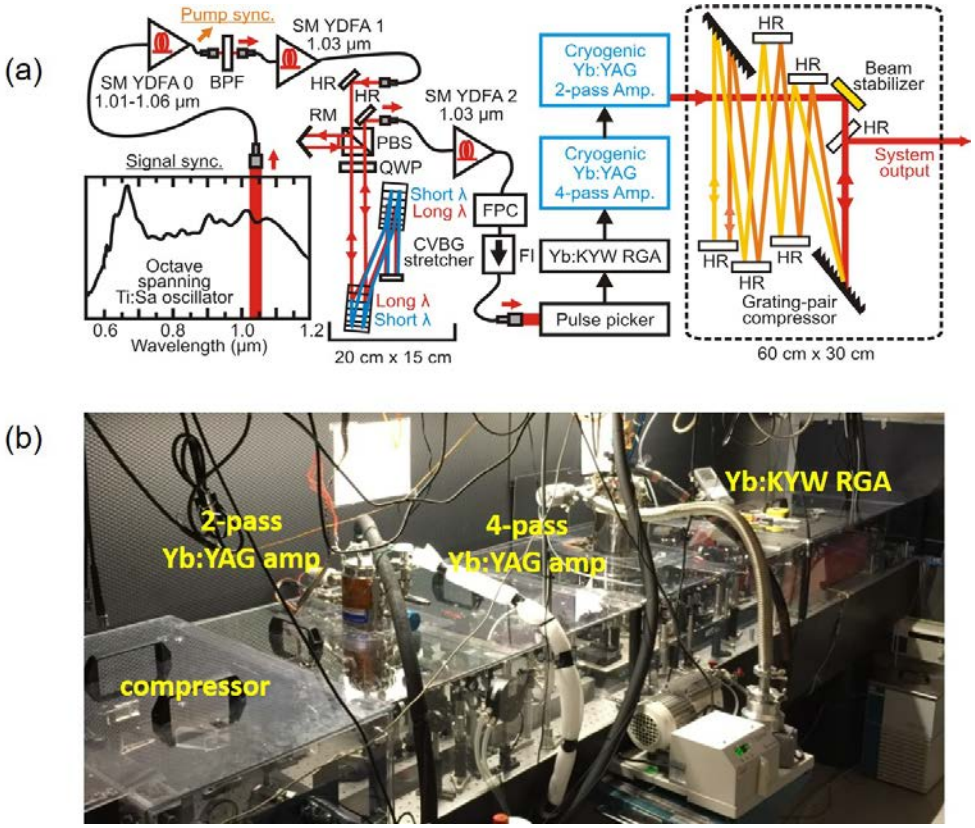

Figure 1: Experimental layout of picosecond hybrid Yb-doped chirped-pulse amplifier laser system (a) and the actual photo of amplifiers (b). SM YDFA, single-mode Yb-doped fiber amplifier; BPF, bandpass filter; HR, high-reflection mirror; RM, roof mirror, PBS, polarization beam splitter; QWP, quarter-wave plate; CVBG, chirped volume Bragg grating; FPC, fiber polarization control; FI, Faraday isolator.

There are three amplifier stages in the Yb-doped CPA chain operating at 1 kHz repetition rate. The first stage is a room-temperature Yb:KYW RGA (s-pulse HP^2, Amplitude Systémes) that provides a bandwidth of ~1 nm much larger than ~0.24 nm of a cryogenic Yb:YAG RGA [Hong10]. This helps to mitigate the B-integral issue in the subsequent amplifiers that induce further gain narrowing and pulse shortening. The second and third stage is a cryogenic Yb:YAG four-pass and

two-pass amplifier, respectively. The more details of this hybrid Yb-doped amplifier chain can be found in [Chang15]. The amplification performance of the two-pass amplifier is summarized in Fig. 2. The amplified energy is 59 mJ at ~160 W of pump power with an extraction efficiency of ~24%. The shot-to-shot energy fluctuations are as low as ~1% rms. The maximum energy is 70 mJ (data point not shown in Fig. 2), but the energy is maintained to be <60 mJ for the safety margin. We were able to maintain 3.5% rms energy stability over 8 hours as shown in Fig. 2(b). This laser is the most energetic picosecond rod-type amplifier at kHz repetition rates.

The laser pulses are compressed using a pair of dielectric-coated diffraction gratings (fabricated by Lawrence Livermore National Lab). The grating groove density and diffraction efficiency of the gratings is 1752 lines/mm and 95%, respectively. The dielectric coating provides a damage threshold of >2 J/cm^2 for ps pulses and a thermal deformation threshold of ~1 kW/cm^2 (CW) within an operation bandwidth of ~10 nm. We set an angle of incidence of 59^o into the first grating and use multiple bounces off additional dielectric mirrors to achieve the required separation of ~4.92 m between gratings in a footprint area of 60 cm by 30 cm. The compressed pulse duration is as short as 6 ps (FWHM) with a throughput efficiency of ~80%. The pulse duration is usually set to 9 ps for OPCPA. Furthermore, the first turning mirror before the pulse compressor is equipped with piezo-electric actuators and is used with an active beam stabilization system (Thorlabs Inc.) to lock the position of the beam at the experiment to reduce the short-term fluctuations of beam pointing and virtually eliminate the long-term pointing drift. As a result, <6 μrad rms beam pointing stability was obtained over 8 hours (Fig. 2(c)).

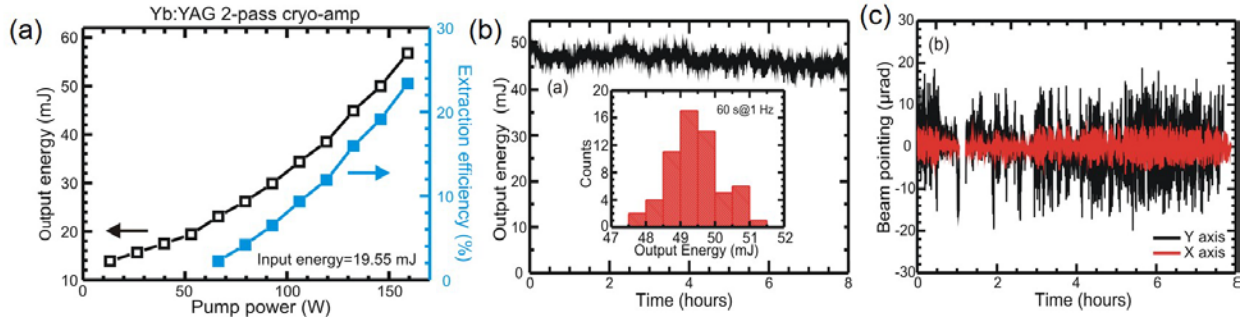

Figure 2: Amplification performance in the 2-pass Yb:YAG amplifier: (a) output energy and extraction efficiency vs. pump power, (b) long-term energy stability measurement at 45 mJ output, and (c) long-term beam pointing stability measurement.

1.2. Multi-mJ, kHz mid-IR OPCPA

Figure 3(a) illustrates the multi-mJ, kHz, 2.1 μm OPCPA upgraded from our previous work [Hong14]. This OPCPA is simultaneously pumped by two lasers operating at a kHz repetition rate: 1) 12 ps, 4 mJ, 1047 nm Nd:YLF amplifier and 2) 9 ps, 50 mJ, 1030 nm hybrid Yb-doped CPA laser described in the previous section. Both pump lasers are seeded by one Ti:sapphire laser oscillator and therefore optically synchronized. The Nd:YLF CPA pumps the first two OPCPA pre-amplifier stages, while the hybrid Yb-doped laser pumps the final OPCPA stage for power amplification. The ~pJ ultrabroadband 2.1-μm pulse is generated via intrapulse difference-frequency generation (DFG), which ensures passive carrier-envelope phase (CEP) stabilization, and is then stretched to ~5 ps by an anti-reflection (AR) coated Si block and amplified in OPA1. Afterwards, it is further stretched to ~9 ps using an acousto-optic programmable dispersive filter (AOPDF; Dazzler, Fastlite) before being amplified in OPA2. Ultrabroadband amplification is

achieved by means of degenerate OPCPA in periodically poled lithium niobate (MgO:PPLN) and periodically poled stoichiometric lithium tantalite (MgO:PPSLT) crystals. A 5-mm-long type-I β-barium borate (BBO) crystal is used for the third OPCPA stage (OPA3), where we obtained a maximum energy of 3.5 mJ. We actively stabilize beam pointing at the BBO crystal using a beam pointing stabilizer for the Yb-doped pump beam, as mentioned in the previous section. The near-Gaussian beam profile, measured after a telescope and the compressor using a pyroelectric camera, reveals excellent quality as shown in Fig. 3(a). The average beam size on both axes is ~12 mm in Gaussian ($1/e^2$) diameter. The compressor composed of two Brewster-angled Suprasil 300 blocks provides a throughput efficiency of 80% including loss in the delivery optics, which can be increased to 90% with a minimal number of delivery optics. The AOPDF not only enables the high-order dispersion compensation but also provides the capability of generating shaped (chirped) pulses that can be used for optimizing control of the HHG process. The spectral bandwidth of the amplified pulses is 407 nm in FWHM centered at 2.1 μm, as shown by Fig. 3(b), and the compressed pulse duration is 26 fs measured with frequency-resolved optical gating (FROG), as shown by Fig. 3(c).

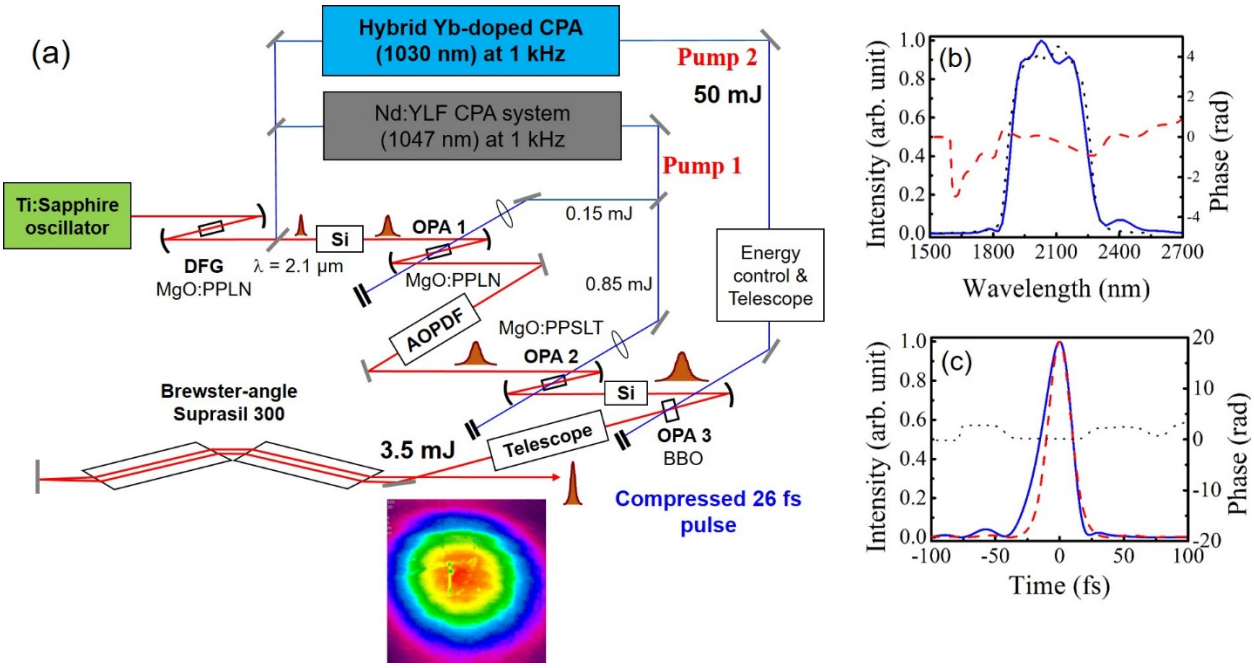

Figure 3: Optical layout of the multi-mJ kHz 2.1-μm OPCPA (a), amplified spectrum (b), and temporal profile measured with FROG (c). The beam profile after compression with a 12-mm Gaussian diameter is also shown in (a). Some dots of the beam profile is owing to the damaged pixel elements with the pyroelectric camera. The blue dotted line in (b) represent the measured spectrum, the blue solid line, FROG-retrieved spectrum, and the red dashed line, spectral phase. The solid blue line in (c) represents the measured temporal profile (26 fs), the red dashed line, the transform-limited pulse, and the dotted black line, temporal phase. All the acronyms are spelled out in the text.

1.3. Water-window soft X-ray generation driven by mid-IR pulses

One of the main goals under this grant is to extend the cutoff energy of attosecond high-harmonic pulses to beyond 200 eV, which cannot be explored using conventional 800 nm Ti:sapphire laser sources. We used our 26 fs, 2.1 μm, multi-mJ pulses to extend of HHG cutoff into the water window range (280-540 eV) in a Ne gas cell. Our experimental setup is illustrated as Fig. 4.

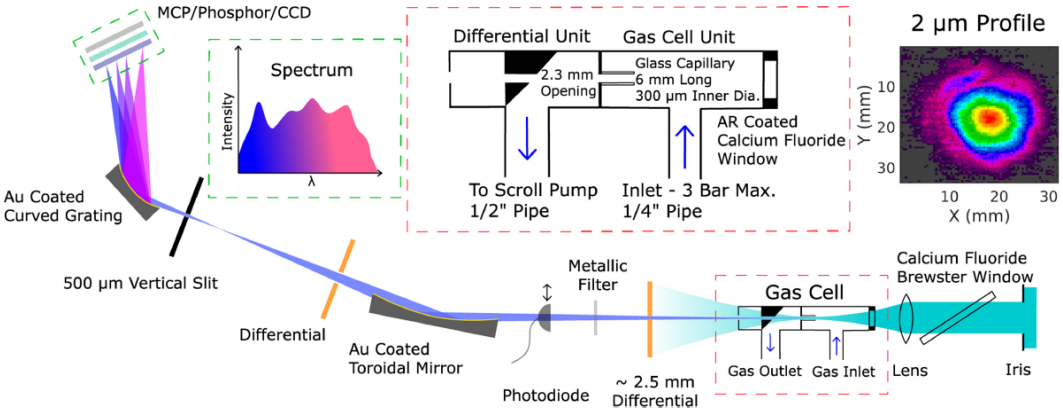

Figure 4. Experimental setup of water-window HHG.

First, measurements on HHG in Ar with lower ionization potential than Ne were conducted to show that our system was functioning correctly, since we have previously demonstrated high-flux soft X-ray HHG in Ar at 60–200 eV [Hong14] using a similar experimental setup but a different gas cell. Consistent with this previous work, the maximum flux occurs for roughly 200 mbar of Ar and required limiting our pulse energy to roughly 1 mJ and tuning the pressure to avoid detrimental plasma effects. This corresponds to a beam waist of ~55 μm and a peak intensity of ~6×10^{14} W/cm^2. Furthermore, we observed that the location of the focus was deep into the capillary, so that the maximum intensity of the beam occurred within 1–2 mm of the vacuum region at the output. Physically, this condition helps to minimize the reabsorption of soft x-ray harmonics and the plasma defocusing of the pulses as they propagate through the gas.

The results on HHG in Ne were collected with 1.35 mJ driver pulses, corresponding to a peak focal intensity of ~1.2×10^{15} W/cm^2, and at a gas pressure of 1.5 bar, which was experimentally observed to maximize the signal on our calibrated, titanium/carbon (Ti/C) coated photodiode (AXUV100Ti-C2 from IRD Inc.). The pulse energy used is less than the peak energy available as it was necessary to adjust the entrance iris when optimizing for HHG conversion efficiency. The spectra for Ne were collected in the presence of two different filters: one comprised of 1 μm of carbon and one of 500 nm of titanium. In addition to obstructing the driver pulse, the spectral responses of the filters also have a rather profound effect on the spectra. The corresponding response curves are shown in the bottom of Figure 5(a). Each spectrum was accumulated over a 100 s integration time.

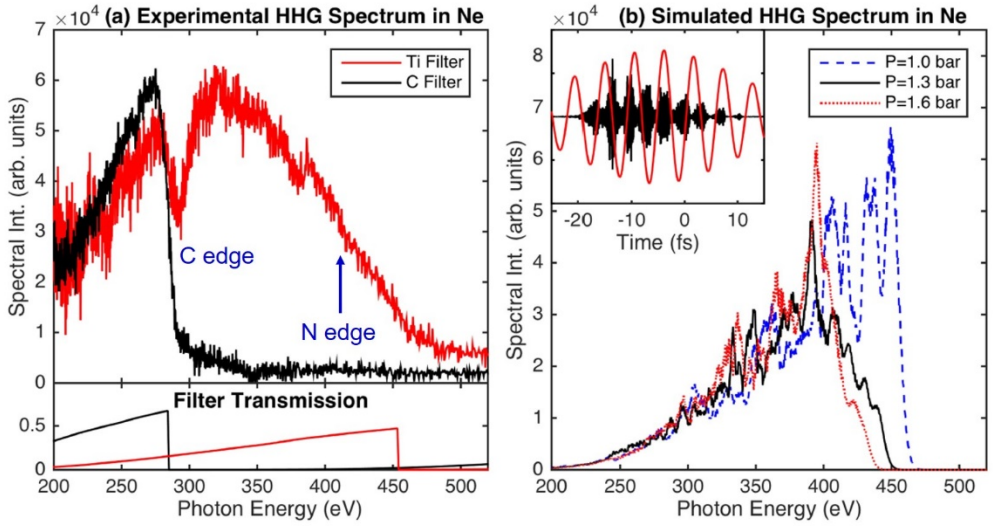

Figure 5. Experimental (a) and simulated (b) spectra of water-window HHG in 1.3 bar of Ne gas. The carbon K-edge at 284 eV is clearly visible and the spectrum collected with the titanium filter shows that we have significant flux within the water window with a cutoff of roughly 450 eV. The spectrum covers the nitrogen K-edge at ~410 eV as well. The filter transmission curves of both the titanium and carbon filters are shown in the panel beneath the experimental data (left). These results are supported by our simulations. In particular, we include three different simulations, at pressures of 1.0, 1.3 and 1.6 bar, showing the effect of changing the gas pressure inside the capillary. Increasing gas pressure results in a lower high harmonic cutoff as stronger plasma defocusing limits the maximum intensity of the beam. The result for P = 1.3 bar most closely matches the experiment. In addition, no metallic filters have been added to the simulation results to emphasize how near to the titanium edge the spectral cutoff occurs. The inset (right) shows the temporal profile of the resultant attosecond harmonic pulse train (black curve) along with the electric field of the 2 μm driving pulse (red curve) for a pressure of 1.3 bar.

As shown in Fig. 5(a), with the carbon filter, we clearly observed the carbon K-edge at 284 eV, demonstrating that the HHG in Ne reached the water-window soft X-ray region. One might notice that the Carbon K-edge is expected to be extremely sharp, though the measured profile is relatively smooth. The full spectrum can be observed as the red curve in Figure 5(a), in which the beam is filtered by a 500 nm titanium filter. The spectrum shows a high harmonic cutoff of roughly 450 eV, which is not only well within the water window but also above the nitrogen K-edge at 410 eV. However, the spectral dip which occurs surrounding 284 eV is indicative of a small amount of carbon contamination in the system. The appearance of carbon is common, if not unavoidable, and roughly totals to only about a 50 nm thick film over the course of the soft X-ray beam's propagation.

Even in the presence of carbon, it is clear that the peak of the spectrum occurs at around 350 eV. An average current of ~18 pA was measured on the Ti/C photodiode, corresponding to a photon flux of ~1.5×10^{6} photons/s/1% bandwidth at the peak energy of 350 eV and ~1.0×10^{6} photons/s/1% bandwidth at the nitrogen edge at 410 eV. Since our beam has to pass through a 2.5 mm diameter aperture between the gas cell and the photodiode, we can determine that our beam divergence is <6.25×10^{-3} sr, and that the generated beam has a brilliance between 10^{6} and 10^{7} photons/(s×0.1%BW×μm^2×sr). The measured flux is comparable or slightly lower than previous reports [Chen10, Cousin14] while the calibration methods are all different. The corresponding HHG conversion efficiency into 1% bandwidth is as low as 10^{-12}–10^{-11}. We believe this can be further increased by optimizing the gas cell geometry considering higher conversion efficiencies reported by other groups. Nevertheless, this is the first demonstration of the water-window HHG up to the nitrogen edge driven by an energy and power scalable kHz mid-IR OPCPA [Stein16].

In an effort to understand our experimental HHG results in Ne gas with high pressure, we ran simulations with a modified numerical model. In close agreement with the experimental parameters, the simulated laser pulses have 32 fs, a focused beam waist of 45 μm and an energy of 1.35 mJ, thereby matching the peak intensity of roughly $1.2x10^{15}$ W/cm^2. In addition, the gas pressure inside the semi-infinite cell, of length 5 mm, is set to P = 1.3 bar and is given a smooth Lorentzian tail at the output (where the beam is focused) to avoid sharp discontinuities. Due to physical constraints, it was not possible to measure the gas pressure inside of the gas cell housing, but, rather, at a location outside of the vacuum chamber. Thus, the pressure inside of the gas cell is slightly less than the measured value. Our simulations indicate that a pressure of 1.3 bar yields the best match to the measured spectra given the laser parameters cited. This result can be compared to spectra for 1.0 and 1.6 bar of Ne, which are also shown in Figure 5(b). The inset of Figure 5(b) shows the corresponding temporal response at 1.3 bar. As expected from the experimental results, the high-harmonic spectrum is effectively bounded below by 250 eV and above by about 440 eV, which is the high-harmonic cutoff energy. At first glance, the agreement between the simulated and experimental spectral shapes is potentially difficult to see, since the filters are not included in the simulation and their spectral features, particularly that of the carbon edge at 284 eV, are missing. In addition, the experimental spectrum appears to peak near its center around 350 eV whereas the simulated spectrum continues to rise. However, small fluctuations in the laser energy, which is typical of systems like ours, results in a shift of the peak energy of the pulse. As such, the aggregate spectrum, which is integrated over many thousands of shots of different energies, cannot be directly matched to any one-shot spectrum, which is produced by the simulations. Attempting to reproduce the full spectrum with the simulations is computationally infeasible. Fortunately, the most significant features of the simulation results match those of the experiments, further supporting the efficacy of the model.

Consistent with the experimental observations, the simulated peak driver intensity occurs very near to the output of the gas cell. Since the high harmonic photons are generated within a very narrow region surrounding this peak intensity, phase matching of the conversion process does not play a significant role in determining the output flux. Enhancement of the flux through phase matching, which would require fine tuning of a host of parameters over an extended distance, remains an elusive goal for the parameter regime of interest here. However, for our current approach, the key limitation to getting higher photon flux is gas handling. After the generation region, any gas causes attenuation of the flux through reabsorption of the high harmonic photons. As such, the creation of a more compact gas cell and better differential pumping mechanisms is a clear path forward to increasing the output flux.

2. Sub-cycle control of soft X-ray HHG using synthesized mid-IR waveforms

Study and sub-cycle control of soft X-ray HHG yield using synthesized waveforms have been the primary goals under this grant. Our earlier theoretical work [Jin14] by co-PI, Lin's group, has revealed that two-color mixed waveforms with ω and 3ω pulses are close to optimal for enhanced soft X-ray HHG. On experimental side, we previously demonstrated an OPCPA-based single-cycle pulse synthesizer [Huang11] by combining CEP-stable 2.1 μm and 800 nm pulses with ~25 μJ of energy. Actually, the waveforms generated by this pulse synthesizer are close to optimal for high-flux soft X-ray attosecond pulse generation up to water-window region. However, we learned that, due to significant engineering challenges, long-term stable operation (over several hours) at mJ level could not be achievable with this synthesizer by the end of Years 2 of this grant. Therefore,

we decided to perform a two-color-driven (ω+3ω, 2.1 μm and 700 nm) HHG experiment to demonstrate enhancement and sub-cycle control of soft X-ray HHG instead of using the 2.1 μm + 800 nm pulse synthesizer. In this study, we used Ar as HHG medium because Ne is much harder to work with due to high pressure for good phase matching. In this section, we describe our experimental and theoretical study of HHG using waveform-controlled mid-IR pulses.

2.1. Efficiency enhancement of two-color (ω+3ω) driven soft X-ray HHG

2.1.1 Experimental setup and procedure

The experimental setup of two-color HHG consists of four main parts: (i) a high-power OPCPA providing the fundamental pulses at 2.1 μm (see Fig. 3), (ii) a dichroic Michelson-type interferometer to control the delay between the fundamental pulse and its third harmonic (700 nm), (iii) a custom-made HHG beamline equipped with a tailored gas cell and different diagnostic tools and (iv) detection units for the generated EUV and soft X-ray light. Fig. 6(a) illustrates the experimental diagram.

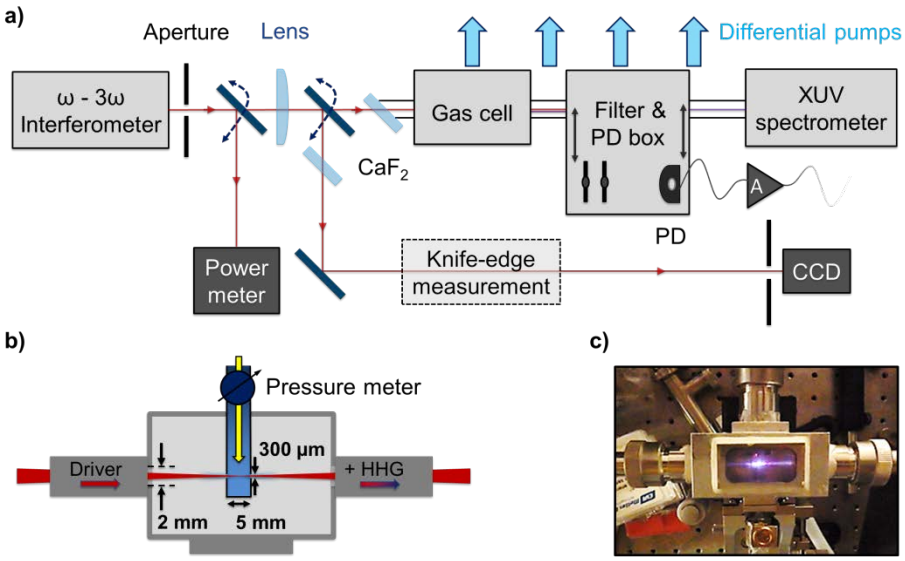

Figure 6: (a) Experimental layout of the HHG chamber and detection systems. A CaF_2 lens focuses the output of the Michelson type two-color interferometer into the gas cell (shown in detail in (b)) and HHG beamline. Different combinations of filters and EUV photo diodes (PD), connected to an electronic amplifier (A), or an XUV spectrometer can be used to characterize the generated high harmonics. Flipper mirrors can send the beam to a power meter or other characterization units such as a CCD camera or traveling-knife-edge stage as well as a BBO crystal to optimize the temporal overlap of the two pulses. (b) Layout of the custom designed gas cell of the HHG beamline. The driving field enters the cell from the left and interacts with the target gas (gas flow indicated by the yellow arrow) at adjustable pressure in the gas capillary (blue). (c) Picture of the Ar-filled gas cell driven by single color pulses from the OPCPA at such power that the generated plasma is visible.

The 1.7 mJ, 26 fs, 2.1 μm pulses (ω pulses) from the 1 kHz OPCPA are frequency tripled in two subsequent BBO crystals via type-I SHG and type-II sum-frequency generation to 700 nm (3ω pulses). Since group velocity mismatch in two BBO crystals is compensated naturally, we obtain a high THG efficiency of ~20 % without an additional delay line for ω and 2ω pulses. The ω and 3ω pulses then enter a Michelson-type interferometer equipped with a custom designed dichroic beam splitter for relative delay control. Residuals of any ω light in the 3ω arm are

deflected to a beam block via a thin ITO plate. The retro-reflector cube in the ω arm was mounted on a piezo motor (PX38 SG, piezosystem Jena) with external controller (NV40/3 CLE, piezosystem Jena) which is used to scan the optical path difference for the pulses in steps of 200 nm (corresponding to temporal steps of 670 as) in closed loop. The rms timing jitter between the two pulses at fixed piezo position was determined to be ~397 as (corresponding to about 17 % of a single cycle of the 3ω pulse) after the interferometer over a duration of 4 s, measured using the interference signal of a helium neon laser with two fast photodiodes in a quadrature detection geometry. The optical components of the interferometer together with the focusing optics before the HHG gas cell add dispersion to both ω and 3ω beams, resulting in slightly chirped pulses of approximately 37 fs and 26 fs duration, respectively.

After passing through an adjustable aperture, the output of the interferometer is focused using a CaF_2 lens (f = 29 cm) through a CaF_2 window into a custom designed gas cell with tunable Ar backing pressure. The gas cell consists of a chamber equipped with a small gas capillary of 5 mm diameter and with holes drilled into its side such that the driving laser field can enter the gas-filled region. In the experiments for HHG, we use three different backing pressures of 375 mbar (optimal pressure for single-color driven HHG), 200 mbar and 143 mbar (lowest pressure yielding signal above noise floor). The beamline is equipped with a differential pumping stage leading to a chamber equipped with 500 nm thick Al- and Zr-filters used to block any residual pump light. In combination with two calibrated EUV photodiodes coated with Al and a Ti-C composition respectively (AXUV100Al and AXUV100Ti/C2, OptoDiode Corp.), the integrated high harmonic flux can be measured either in the range of ~20 – 73 eV or 85 – 205 eV. A low-noise electric amplifier (DDPCA-300, FEMTO Messtechnik GmbH) amplifies the photodiode (PD) signal. Harmonic spectra are measured with an EUV/SXR spectrometer. For improved signal-to-noise ratio vertical binning of the CCD was employed and the entrance slit of the monochromator was fully opened to a width of about 500 µm. The acquisition time of the thermo-electrically cooled CCD (– 40 °C) is set to 20 s (at 375 mbar) or 30 s (at 200 mbar and 143 mbar).

The two pulses are checked to overlap temporally via sum-frequency mixing in a BBO crystal, while their spatial overlap at the focus was measured via the traveling knife-edge technique for the fundamental and with a CCD camera (WinCamD UCD23, DataRay Inc.) for the third harmonic. This way, the beam radius ($1/e^2$) is determined to be ~55 µm for the ω-beam and ~30 µm for the 3ω beam with the aperture set to a diameter of 7 mm.

The experiments were carried out under the following procedure: First, the single-color-driven HHG signal on the Al-coated PD was maximized using the adjustable iris and the position of the CaF_2 lens before the gas cell. The optimal aperture diameter was found to be about 7 mm which resulted in pulse energies of ~360 µJ (ω) and ~36 µJ (3ω), respectively. The corresponding peak intensities at the focus thus were ~2.1×10^{14} W/cm^2 and ~9.6×10^{13} W/cm^2. The focus of the beams was set towards the rear end of the gas capillary and the interaction length was estimated to be approximately 3 mm. Before adding the 3ω beam, we collected the single-color driven HHG data both with the PD's and the spectrometer to later compare them with the two-color driven HHG data. To measure one full spectrum ranging from 35 to 220 eV we had to scan the CCD detection stack to four different positions on the Rowland circle of the EUV/SXR spectrometer. Once the single-color data was recorded, the third harmonic was added. Now we started scanning the relative delay. The piezo-motor in the interferometer was scanned while spectra or integrated yield were measured at each position. We used two filters, 0.5-µm-thick Al and Zr, to cover the whole spectral range of the generated high harmonics. The delay scans were performed with one filter first, before being repeated with the other. This allowed faster data acquisition, minimizing

effects due to temperature drifts in our lab (scale of ~10 minutes). The downside of this procedure is that the two-color-driven HHG spectra obtained at different CCD positions are hard to be directly stitched together over the whole energy range of 30 to 220 eV, as a slight offset of relative delay could be introduced with the open-loop interferometer. This procedure, which is fully automated, was then repeated for each pressure.

2.1.2 Experimental results

HHG spectra have been measured with different relative phases over 4 different spectral ranges covering 35 – 210 eV. As an example, HHG spectra at 200 mbar Ar pressure are shown in Figs. 7(a) – (d). As mentioned before it should be noted the spectra are not directly stitched together because the relative delay scan was made at each spectral region and the reference zero delay might slightly drift for different spectral ranges. Since argon is strongly absorbing in the range of 16 – 40 eV, reabsorption after the gas capillary causes the recorded spectra to be measurable starting at around 40 eV [Henke93]. The intensity of the 3ω pulse is high enough to generate harmonics by itself, but the cutoff of 3ω-driven HHG does not reach beyond ~30 eV and therefore is not experimentally observed. The individual harmonics shown in Fig. 7 are well resolved for photon energies up to ~50 eV, whereas the resolution is not sufficient beyond that energy due to the fully opened entrance slit in the monochromator.

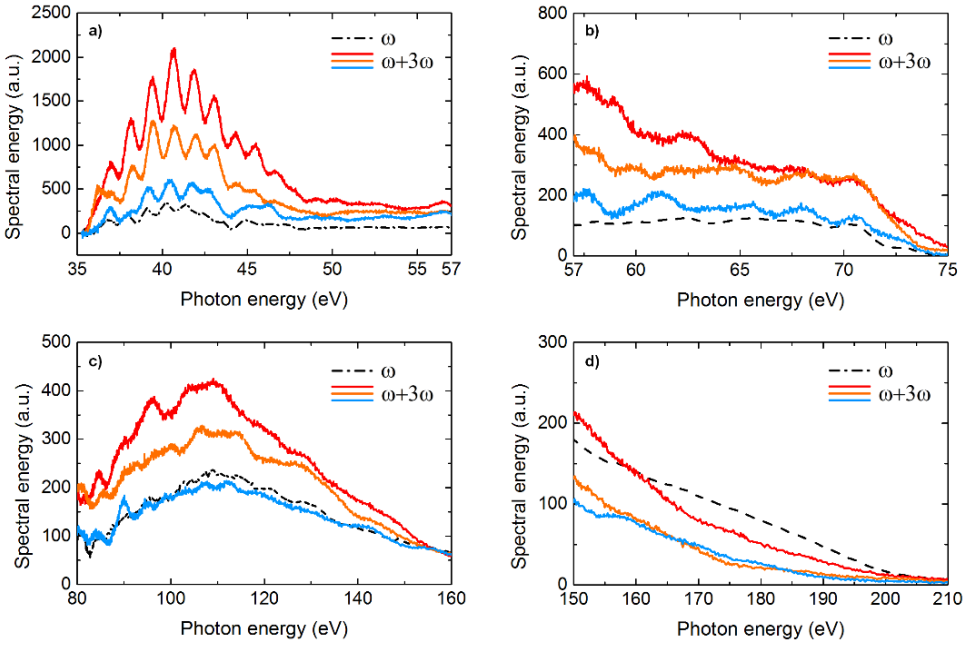

Figure 7: Selected two-color (ω+3ω) HHG spectra measured within one modulation period of the two-color waveform when scanning the two-color relative phase at a backing pressure of 200 mbar. The spectra were chosen as such to show the magnitude of modulation caused by scanning the ω-3ω delay. For comparison the corresponding single-color (ω) driven spectrum is shown in black.

The recorded spectra in Fig. 7 inhibit a strong modulation of harmonic intensity with the two-color phase at a periodicity matching the period of the 3ω control pulse. We show the HHG spectra for three different relative phases within one modulation period for each spectral region. The dependence of the HHG spectral intensity on the relative phase is the strongest in the region below 60 eV. While significant enhancement compared to the single-color driven HHG level is

observed at lower photon energies, this enhancement decreases towards higher photon energies. The same holds for the strength of the modulation imposed on the spectral intensity as a function of relative two-color phase. The modulation of harmonic yield is clearly visible in the integrated enhancement measured with the PDs as well, which is shown in Fig. 8. The enhancement given by the recorded photo-current normalized to the single-color driven photo-current is periodically dependent on the relative delay of ω and 3ω pulses, as already observed in the spectra. The clear modulation with the optical cycle of the 3ω control field proves that the HHG process is manipulated at sub-cycle precision via changes in the relative delay (or relative phase near zero delay) of the two-color waveform [Kroh16].

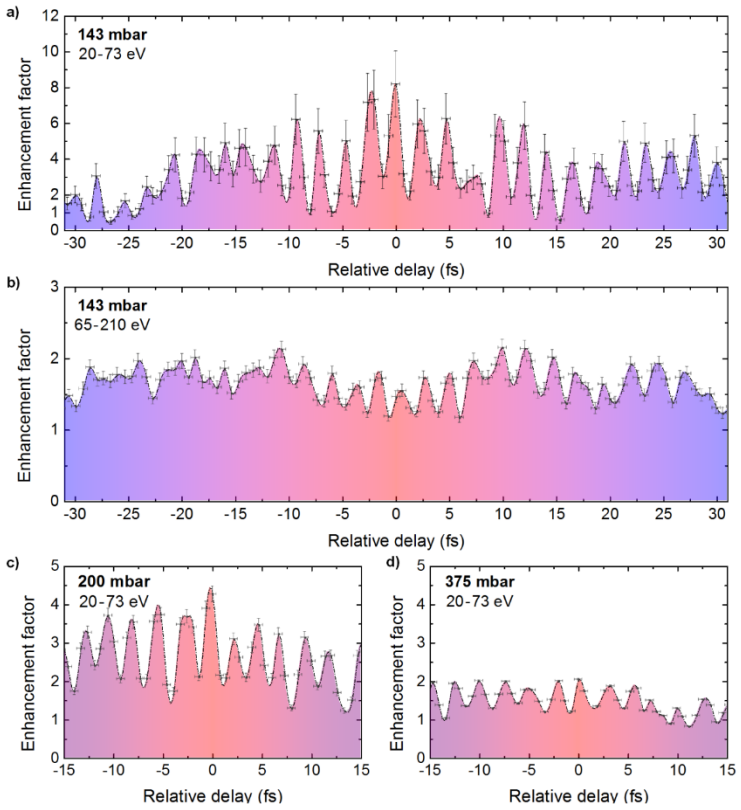

Figure 8: Average enhancement factors given by the measured ω+3ω EUV photodiode currents normalized to the single-color ω-driven signal. At each pressure the data was recorded for each position the piezo motor in the two-color interferometer was moved to in order to scan the relative delay between ω and 3ω. (a) and (b) show the enhancement factors integrated over photon energies between approximately 20–73 eV (shown in (a)) and for approximately 85 – 205 eV (shown in (b)) at 143 mbar of argon pressure. Figure (c) and (d) show the PD signals zoomed in to the region around 0 fs delay for the 20 – 73 eV region for 200 mbar and 375 mbar Ar pressure, respectively.

From Figures 8(a) and (b) which show the enhancement measured at 143 mbar we can find that both the maximum enhancement and the magnitude of the modulation are lower at higher photon energies, which agrees with the observation from the HHG spectra. At low photon energies measured with the Al-coated PD (20 – 73 eV), as shown in Fig. 8(a) for 143 mbar, (c) for 200 mbar and (d) for 375 mbar, the maximum enhancement can be found at the region of zero delay between ω and 3ω pulses, whereas the enhancement at the high energy side measured with the TiC_2-coated PD (85 – 105 eV) shows a mild dip near zero delay. This feature is attributed to the fact that at

zero delay the peak intensity is maximal and as such the ionization rate. Consequently, the dispersion introduced by generated free electrons is maximal and therefore degrades phase-matching. The phase mismatch has more dramatic impact on higher energetic HHG photons, as phase-slippage of the generated harmonics with respect to the driving waveform is larger. Additionally, the driving waveform itself suffers from dispersion which leads to an effective reshaping of the two-color waveform throughout its propagation through the interaction volume. This can be seen as an intrinsic scan of the two-color phase along the propagation, which effectively results in the detector averaging over several two-color phases. This averaging then reduces the magnitude of modulation.

Figure 8 indicates that the degree of modulation of the enhancement is also dependent on the target gas pressure and not only on the HHG photon energy. For increasing pressure the degree by which the enhancement is modulated via the two-color phase decreases. The higher photon energies are affected more severely and the traces recorded for 85 – 205 eV at 200 mbar and 375 mbar don't show a significant degree of modulation anymore.

Although 375 mbar marks the optimum pressure for the single-color driven case, we find the maximal observed enhancement by the added 3ω pulse to be the lowest at this pressure. Table 1 shows the maximal integrated enhancement factors recorded throughout the PD scans for each pressure, where the enhancement factors both measured between 20 – 73 eV and 85 – 205 eV drop with increasing argon pressure. The drop of enhancement is observed to be more dramatic for the low energy, which reduce from a maximum of ~8 at 143 mbar to a factor of ~2 at 375 mbar. At higher photon energies, where the enhancement is less pronounced anyway, the value hardly drops between 143 mbar and 200 mbar and shows reduced photocurrent levels for all two-color delays at 375 mbar with a maximum reachable flux at only about 90 % of the single color level.

	Al-coated PD (20 – 73 eV)			**TiC_2-coated PD (85 – 205 eV)**		
p (mbar)	**I_ω (pA)**	**$I_{3\omega}$ (pA)**	**Enhancement**	**I_ω (pA)**	**$I_{3\omega}$ (pA)**	**Enhancement**
143	0.27	2.24	8.2	5.56	11.94	2.2
200	1.23	5.27	4.3	9.97	20.82	2.1
375	6.87	14.06	2.0	67.07	60.50	0.9

Table 1. Maximal enhancement factors of the integrated HHG yield between approximately 20 – 73 eV measured with the EUV Al-coated photodiode and for 85 – 205 eV measured with the EUV TiC_2-coated photodiode for different pressures of argon. The background corrected average single-color currents I_ω are given as well as the maximum current $I_{3\omega}$ of each delay scan of the two-color experiment.

2.1.3 Comparison with simulations

For the comparison of the experimental results with simulations taking realistic conditions into account the Maxwell wave equations were solved in 3D using a quantitative-rescattering (QRS) based single atom response [Jin2014]. The parameters were chosen as such to match our experiment and setup as close as possible: the parameters for the fundamental field were chosen as 2.1 µm center wavelength, 37 fs pulse duration (5.3 cycles) with a pulse energy of 360 µJ and a beam waist of 55 µm. For the 3ω control pulse parameters the wavelength was set to 700 nm with a duration of 26 fs (11.1 cycles), a pulse energy of 36 µJ and a beam waist of 30 µm. The gas cell was modeled at the focal region with an effective length of 3 mm, which matched the experimental observations best. We first ran simulations with chirp-free 36 fs, ω and 26 fs, 3ω pulses. The relative phase between ω and 3ω pulses was scanned in the range between 0 and 2π. The simulated HHG spectra at three different Ar pressures, 76, 106, and 200 mbar, are shown in

Figs. 9(a), (b), and (c), respectively. It should be noted that from the simulation the single-color optimum occurred at 200 mbar which is about factor 2 less than the backing pressure used in our experiment. Since the accurate experimental characterization of the pressure at the interaction region is difficult, we scaled the pressure accordingly by factor of two. Also, in our previous works with different gas cells [Hong14, Stein16] the optimal backing pressure for Ar at the same drive wavelength was consistently ~200 mbar. Therefore, it is conceivable that the current gas cell geometry offers ~factor of 2 lower pressure at the interaction region than backing pressure. For this reason, the experimental HHG data at 375 mbar of backing pressure is compared with 200 mbar in simulation, 200 mbar of backing pressure, with 106 mbar in simulation, and 143 mbar of backing pressure, with 76 mbar in simulation. The simulated HH spectra in Fig. 8 clearly show consistency to our experimental observations: 1) harmonic yields are sensitive to the relative phase, 2) higher enhancement is observed at lower energy, and 3) higher enhancement factor is observed at lower pressure. However, the enhancement factor is a few times overestimated in the simulation.

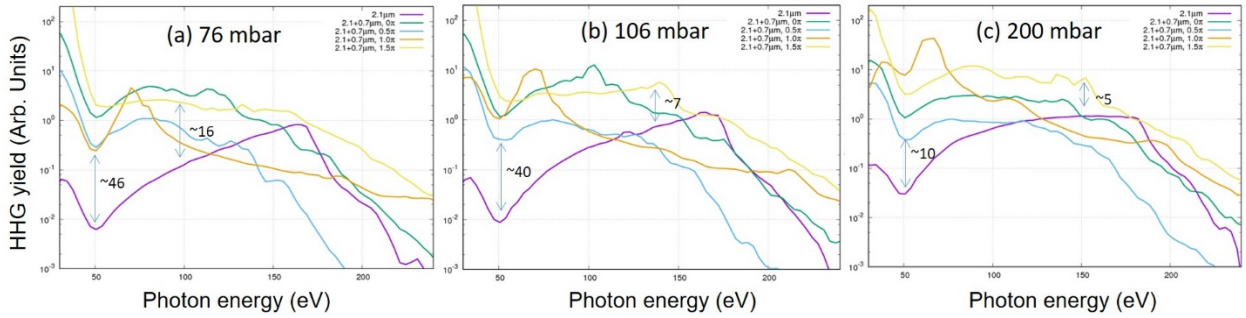

Figure 9: Simulated HHG spectra with different relative phases at different pressures, (a) 76, (b) 106, and (c) 200 mbar. The spectra are all smoothened for clear representation of yields. Transform-limited 36 fs of ω pulse and 26 fs of 3ω pulse are used for driver.

We further investigated the effect of laser chirp on the enhancement. Figures 10(a) and (b) shows the HHG spectra at 106 and 200 mbar, respectively, driven by positively chirped 36 fs, ω and positively chirped 26 fs, 3ω pulses. While the general tendency was preserved, we observe smaller enhancement factors than the chirp-free cases in Fig. 9. The positive chirp seems to increase the harmonic efficiency of the single-color case at the cost of slight cutoff reduction. Overall experimental scenario is more clearly explained with the positive chirp of driving pulses.

It should be noted that calculated ionization rates with two-color cases are much higher than optimal single-color cases at each pressure, which is found to make the phase matching at high energy with two-color drivers more difficult and even reduce the harmonic yield at a certain relative phase. That being said, two-color-driven HHG has both promises and challenges in increasing the harmonic efficiency. Global optimization of experimental parameters including the two-color laser intensity and phase matching condition is necessary.

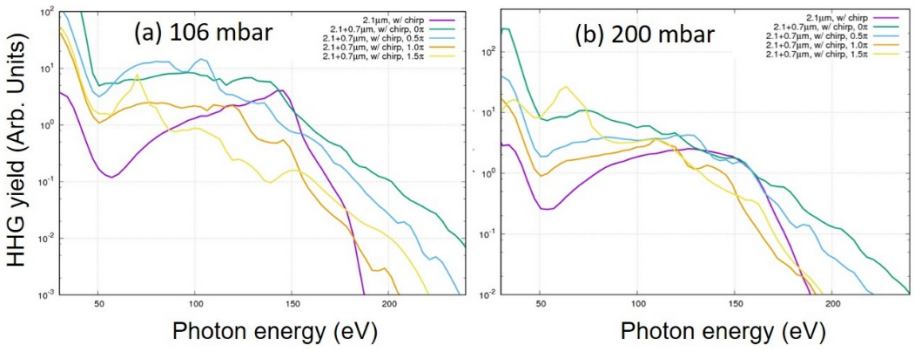

Figure 10: Simulated HHG spectra with different relative phases at different pressures, (a) 106 and (b) 200 mbar. The spectra are all smoothened for clear representation of yields. Chirped 36 fs of ω pulse and 26 fs of 3ω pulse are used for driver. Overall enhancement is reduced compared to the transform-limited case in Fig. 9.

Our work suggests that for high-pressure gas HHG setups (e.g. using helium), which need multiple differential pumping stages to maintain the vacuum level for the detection, two-color driving schemes open the perspective of reducing the target gas pressure while maintaining the flux-level of the high harmonics. For further extension of the enhancement to higher photon energies considerable effort will have to be put into the stabilization of the driving waveform first, which is also a problem current optical synthesizer are facing. Future work may thus be dedicated to this problem and focus on finding a global macroscopic optimum for each driving waveform. At stabilized conditions a two-color approach using even longer driving wavelengths in the mid-IR is expected to boost the spectral content in the plateau region of the HHG spectrum – possibly up to the water window regions.

2.2. Theoretical study of optimal HHG

High harmonics are generated from all the atoms in the gas medium coherently. They depend on the nonlinear macroscopic propagation of the fundamental laser beam together with the high-harmonic field. A full description of experimentally observed HHG spectra consists of two parts: (i) the single-atom response; that is, the induced dipole by the driving laser field which can be obtained by solving the time-dependent Schrödinger equation (TDSE) or by some equivalent simpler models; and (ii) the macroscopic response, through solving the three-dimensional Maxwell's equations of the fundamental laser and the high-harmonic fields.

In the last three years, we have been focusing on how to improve the characteristics of high harmonics in the different spectral regions from both the single-atom and the macroscopic aspects, by optimizing the macroscopic parameters, the multi-color laser waveform, and by increasing the gas pressure in a high-ionization medium.

2.2.1 Optimal HHG by adjusting macroscopic conditions

The hollow waveguide is a commonly used experimental setup for HHG, which has been implemented for creating quasi-phase matching (QPM) conditions, selecting electron trajectories, temporally and spatially shaping the driving laser pulse, combining with a ultraviolet (UV) laser to efficiently producing soft X-ray harmonics, and generating keV harmonics with mid-IR lasers. In a hollow waveguide, the diffraction effect can be eliminated such that spatially constant laser intensity can be maintained over an extended distance and the geometric phase does not depend on the radial distance. This is considered to be an ideal setup to keep a nearly constant waveform as the laser pulse propagates. We have proposed to combine two advanced technologies: multi-color laser pulse synthesizer and laser guiding in a waveguide, to generate extremely bright high

harmonics and isolated attosecond pulses in the soft X-ray region. This goal has been achieved by optimizing waveguide parameters (radius and length) and gas pressure. We have also demonstrated that the harmonic yield and divergence can be scaled to different focusing geometries.

a. Generation of spatially coherent soft X-ray high harmonics

We have investigated the efficient generation of low-divergence high-order harmonics driven by two-color optimized laser pulses in a gas-filled hollow waveguide. In Fig. 11(a), the total harmonic yields generated by the two-color waveform are shown at the optimal conditions. These conditions ensure that highest cutoff energy and highest harmonic yields are achieved simultaneously. The harmonic yields from a reference 1.6-μm laser are also shown, which is about 1 to 2 orders of magnitude smaller than the two-color pulse. The harmonic emissions in the far field for the two cases are shown in Figs. 11(c) and 11(d). Two-color high harmonics in the spectral range of 70 to 250 eV are well localized along the propagation axis with divergence angle smaller than 1 mrad. If one uses an aperture to filter out divergent harmonics (> 1 mrad), the results in Fig. 11(b) show that two-color high harmonics are more than three orders of magnitude larger than the single-color ones. Further theoretical analysis uncovered that under the optimal waveguide parameters and gas pressure, the balance between waveguide mode, atomic dispersion, and plasma effect could be reached to achieve dynamic phase matching and that the optimized two-color waveform was maintained throughout the whole hollow waveguide [Jin15PRL].

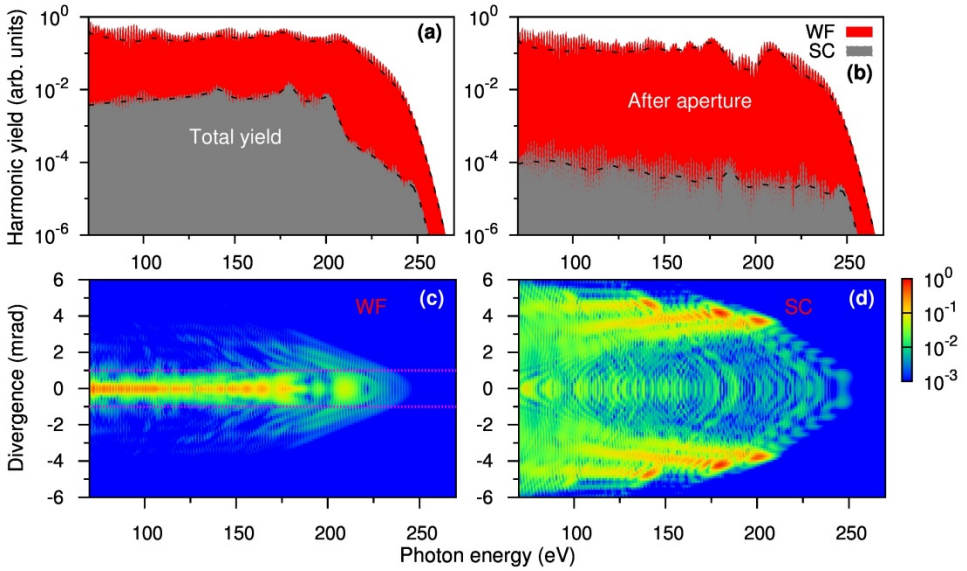

Figure 11: (a) Total harmonic yield emitted at the exit of the hollow waveguide, and (b) harmonic yield integrated within 1 mrad using an aperture in the far field for two-color (1.6+0.533 μm) waveform (WF) and single-color (SC) laser. The corresponding harmonic divergence in the far field for WF (c) and for SC (d). Length and radius of the waveguide are 5 mm and 125 μm, respectively, and gas pressure is 50 Torr. Adapted from Ref [Jin15PRL].

b. Generation of spatially coherent soft X-ray isolated attosecond pulses in the far field

We have demonstrated numerically the generation of intense, low-divergence soft X-ray isolated attosecond pulses (IAPs) in a gas-filled hollow waveguide using synthesized few-cycle two-color laser waveforms. The waveform is a superposition of a fundamental and its second harmonic optimized such that highest harmonic yields are emitted from each atom. We then optimize the gas pressure and the length and radius of the waveguide such that bright coherent high-order harmonics

with angular divergence smaller than 1 mrad are generated, for photon energy from the extreme ultraviolet to soft X-rays.

In Fig. 12(a), we show three near-field soft X-ray attosecond pulses. To check the spatial quality of the IAP in the far field and the effect of harmonic propagation in the vacuum, we show the far-field IAPs in Fig. 12(b). The spectral range used to synthesize the IAP is the same as the near-field one. For IAPs centered around 0.3, 0.1, and 0.6 optical cycle (of 1.6 μm), the angular divergence in the far field was chosen to be 2, 1, and 1 mrad, respectively. We can see from this figure that (i) the intensity of the IAP in the far field is comparable to or even greater than that in the near field, and (ii) the duration of the IAP is close to or even shorter than that in the near field. This example demonstrates that high-intensity and low-divergence soft X-ray IAPs are generated in the far field [Jin16SR].

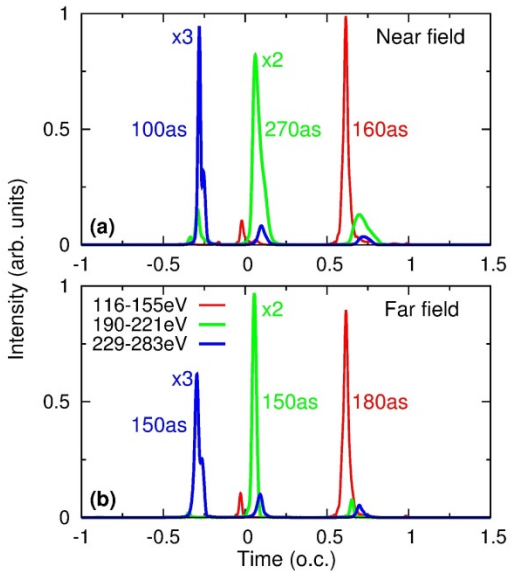

Figure 12: IAPs at (a) near, and (b) far field after high harmonics have been spectrally filtered in the photon energy ranges indicated. The near-field IAPs are integrated over the whole exit plane. Far-field IAPs are integrated within 2, 1 and 1 mrad from left to right in (b), respectively. This indicates that the aperture size can control the spectral range of the high harmonics. The optimal macroscopic conditions are: gas pressure of 70 Torr, waveguide length of 5 mm and radius of 125 μm. Two-color waveform (1.6+0.8 μm) was used. (o.c. means the optical cycle of 1.6-μm laser). Adapted from Ref [Jin16SR].

c. Macroscopic scaling of high harmonics generated in a hollow waveguide

We have demonstrated that the divergence of high harmonics is inversely proportional to the waveguide radius and harmonic yields are proportional to the square of the waveguide radius when the gas pressure and waveguide length are properly chosen to meet the phase-matching condition. The harmonic emissions in the far field and the total harmonic yields at three different focusing geometries are shown in Fig. 13, which shows the scaling of harmonic divergence and yield [Jin17PRA].

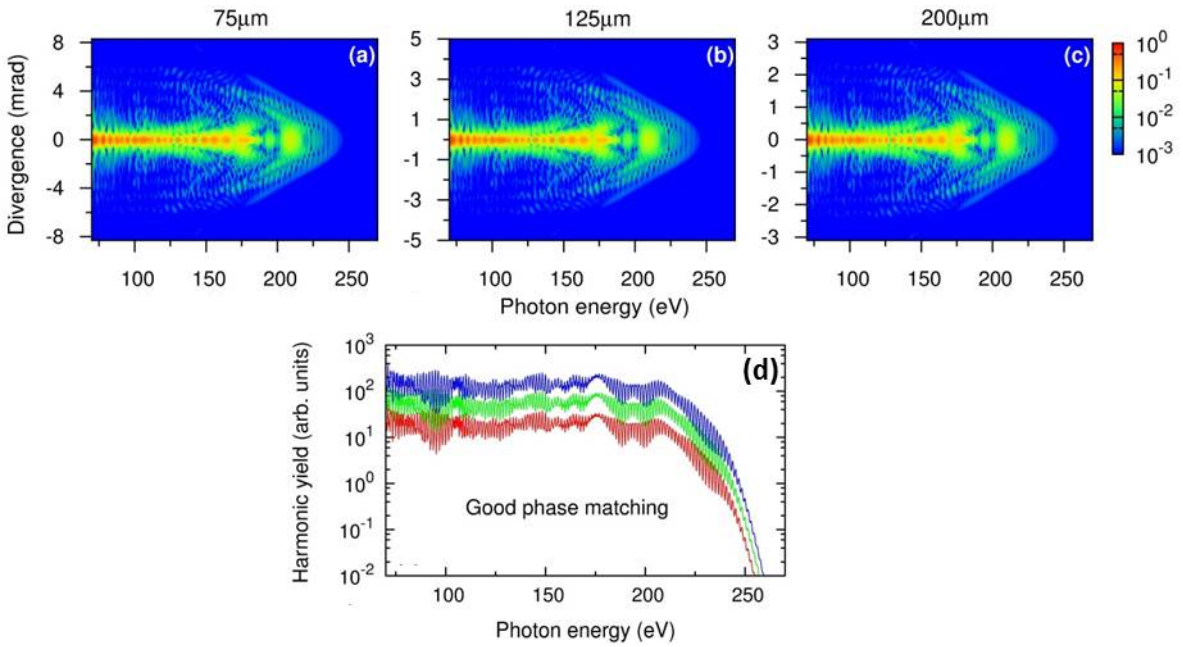

Figure 13: Harmonic emission (normalized) in the far field using the two-color (1.6+0.533 μm) waveform as the initial on-axis laser pulse. The incident beam size is adjusted to ensure that the fundamental EH_{11} mode is guided. The waveguide radii are indicated on the top of figures. (d) Total harmonic yields integrated over the radial distance for harmonic emissions in (a)-(c). Adapted from Ref [Jin17PRA].

2.2.2 Synthesized waveforms for enhancing the yields of water-window HHG

Current wavelength-tunable, CEP-stabilized mid-IR OPAs are mostly pumped by 800-nm Ti:sapphire lasers, thus the mid-IR pulse energies are smaller than pump lasers. An alternative method for enhancing the harmonic yields in the single-atom response is to synthesize an intense 800-nm laser pulse with a relatively weaker, long-wavelength, mid-IR pulse. The wavelength of the latter was optimized, and it could be incommensurate with 800 nm. The optimization was performed over the whole laser pulse (FWHM duration was assumed as 21.3 fs, eight optical cycles of the 800-nm laser) instead of a single cycle.

The optimized laser parameters were obtained for the cutoff energy from 200 to 550 eV covering the "water-window" region. The peak intensity of the 800-nm laser was always about 2.0×10^{14} W/cm^2, the wavelength and intensity of the mid-IR pulse increased monotonically with the increase of the cutoff energy, and the relative phase was quite stable [Jin15OL]. For the cutoff energy of 350 eV, four different simulations with nearly identical total pulse energy are shown in Fig. 14(a). Clearly, a single 1925-nm laser can reach the required cutoff, but with the yield about 1000 times weaker than the 800-nm one. With the two-color waveform, by combining 800-nm and 2126-nm laser pulses, where the latter has about 50% of the energy of the former, the HHG yields over the same spectral range can be increased by about 30 to 100 times with the comparable total laser energy. The one with 1625 nm (3.88×10^{14} W/cm^2) plus its third harmonic gives the highest yields, however, they are only a factor of two or four larger than those in the current scheme, while the total power is slightly larger. The three-color scheme has also been checked. The simulations in Fig. 14(b) show that adding one more color does not help further enhancing the harmonic yields significantly.

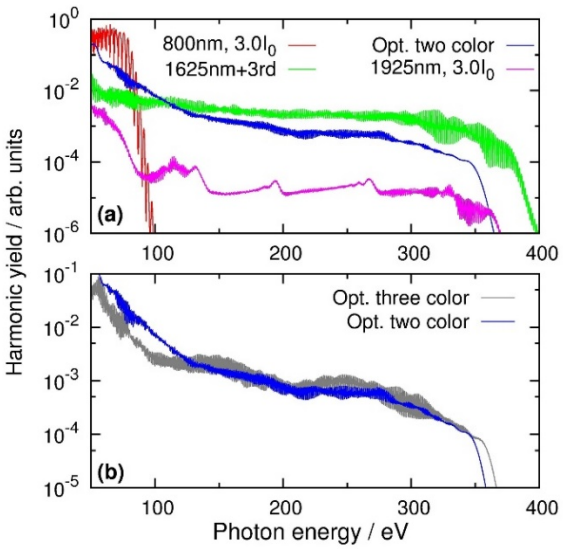

Figure 14: Macroscopic HHG spectra of Ne calculated by the QRS model. (a) Two-color (800 + 2126 nm) waveform in the current scheme is compared with the previous two-color waveform (mid-infrared laser and its 3rd harmonic). One-color results are shown for reference. (b) Comparison of the harmonic spectra by optimized two-color (800+2126 nm) and three-color (800+2356+400 nm) waveforms. Adapted from Ref [Jin15OL].

2.2.3. High harmonic generation under extreme conditions

We have investigated the gas-pressure dependence of macroscopic harmonic spectra generated in a high-ionization medium using intense 800-nm laser pulses. The simulated macroscopic HHG spectra of Ne atoms by varying the gas pressure from 50 to 600 Torr are shown in Fig. 15(a). We can see that with the increase of gas pressure the harmonic cutoff energy gradually decreased and harmonic yields in the plateau progressively increased. The balance between harmonic yield and plateau spectral range is best reached when the gas pressure is 300 Torr, which is taken as the optimal pressure. As shown in Fig. 15 (b), the harmonics obtained at the optimal pressure show good spatial coherence with small divergence (less than 2 mrad) in the far field. By analyzing the evolution of the laser's electric field as it propagates, we find that dynamic phase matching conditions are fulfilled in the second half of the gas cell and that harmonic yields do not depend on the position of the gas cell with respect to the focusing position [Jin16PRA].

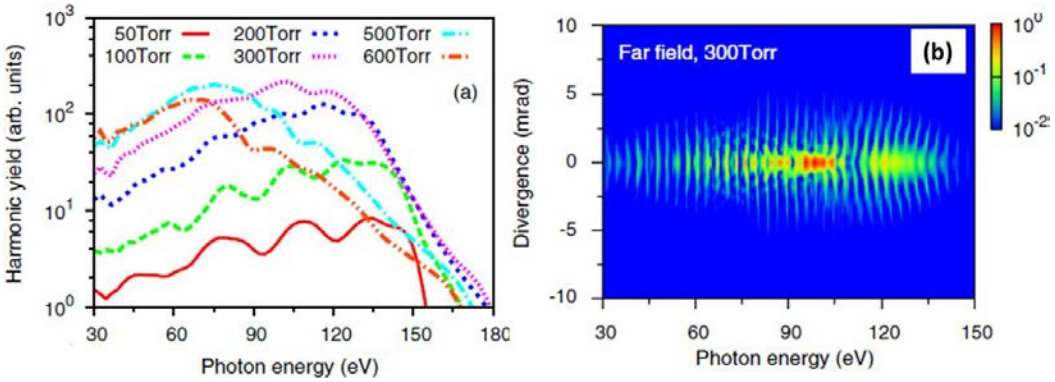

Figure 15: (a) HHG spectra generated in high-pressure neon gas with high-intensity 800-nm laser pulses versus gas pressure. Optimal pressure for the highest harmonic yields is found at 300 Torr. (b) Harmonic emissions with the low divergence in the far field at 300 Torr. Adapted from Ref [Jin16PRA].

3. Mid-IR laser filamentation

Besides the soft X-ray HHG in gases, our 2.1 μm, 26 fs pulses from OPCPA are an excellent source of generating femtosecond mid-IR laser filaments in solids and ambient air due to their high peak power and short pulse duration. In this project, we first studied mid-IR laser filamentation in solids with different dispersion characteristics and demonstrated multi-octave-spanning continuum generation in normal (positive) group velocity dispersion (GVD) medium and self-compression to sub-two-cycle duration in anomalous (negative) GVD medium. Second, we applied it to ambient air and demonstrated mid-IR laser filamenation at kHz repetition rates for the first time [Liang16], which can potentially be used for standoff detection of atmospheric chemicals. There was only a sole demonstration of mid-IR laser filamentation in air at 20 Hz [Mitrofanov15] prior to our work. We describe these efforts in the following subsections.

3.1 Mid-IR laser filamentation in solid materials

In Year 1, we systematically investigated mid-IR super-continuum generation (SCG) from filaments in different dielectrics in both normal and anomalous GVD regimes. CaF_2, BaF_2, and ZnS, which have relatively flat dispersion around 2 μm are chosen as bulk dielectric materials. The bulk dielectrics are pumped by a ~10 μJ, 2.1 μm, 26 fs pulses taken from the second stage of the multi-mJ OPCPA. The continuum spectrum is extended to wavelengths up to ~3.4 μm in CaF_2 and ~4 μm in BaF_2, both in the anomalous GVD regimes. Moreover, we performed SCG in a ZnS crystal with normal GVD. The generated SC spans from 500 nm to 4.5 μm, corresponding to 3.1 octaves, as shown in Fig. 16(a). A stable and robust single filament with a conical far-field profile is formed in ZnS (Fig. 16(b)), despite the pump peak power of 1000 times its critical power. The SC from the filaments not only has broad spectrum but also has few-cycle pulse width and good temporal profile in the anomalous GVD regime. Figure 16(c) shows the temporal profile of the generated mid-IR SC from CaF_2 in the anomalous GVD regime, characterized using a second-harmonic generation FROG technique. The pulse is self-compressed to 13.5 fs in FWHM, corresponding to ~1.8 cycles [Liang15], at ~2.25 μm central wavelength. The pulse is CEP stable and close to transform limited because of the balance between self-phase modulation (SPM) and anomalous GVD.

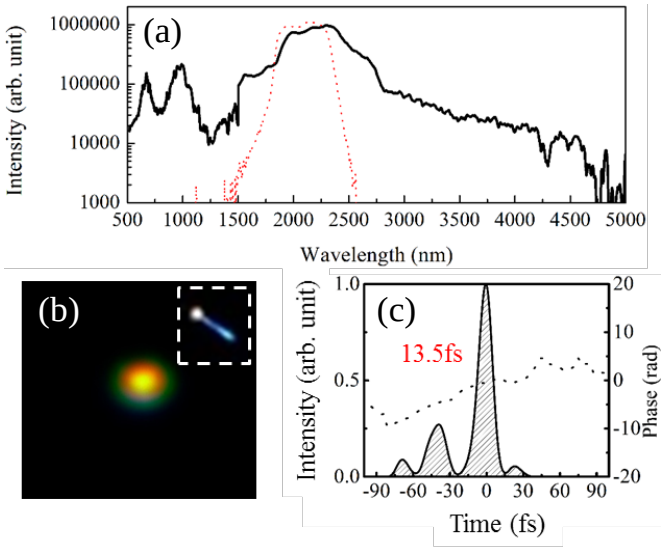

Figure 16: Mid-IR laser filaments in solids. (a) 3-octave-spanning SCG and (b) the spatial profile from ZnS in the normal GVD regime. The sub-2-cycle self-compression of mid-IR pulses in CaF_2 in the anomalous GVD regime (c).

3.2 Mid-IR laser filamentation in ambient air at a high repetition rate (1 kHz)

In Year 2, mid-IR laser filamentation in air was demonstrated using 2.1 μm, 1.7 mJ, 30 fs pulses at 1 kHz repetition rate, delivered from the 3-stage OPCPA. The peak power (~56 GW) is higher than the critical power at 2.1 μm (~45 GW). A CaF_2 lens with focal lengths ranging from 100 mm to 1000 mm is used to focus the beam with a diameter of ~10 mm. A single laser filament is formed in air [Liang16]. For example, the image of ~50-mm-long filament with an *f*=300 mm lens is shown in the inset of Fig. 17(a), where the confocal parameter without filamention is only ~4.6 mm. The length of the filament is expected to be longer with the full energy (>3 mJ) pump. Dramatic spectral broadening from mid-IR to UV occurs from the filamentation as shown in Fig. 17(a) (*f*=300 mm). Odd harmonics up to ninth order are generated, corresponding to ultraviolet (UV) extension to 230 nm. At the same time the octave-spanning continuum is obtained on the mid-IR side. This entire feature is quantitatively reproduced by numerical simulations based on the unidirectional pulse propagation equation (UPPE) model [Suppl. of Liang16], as shown in Fig. 17(b).

The efficiency of third-harmonic (TH), fifth-harmonic (FiH), and seventh-harmonic (SVH) is measured with different focusing geometries. The focal length optimal for the maximum harmonic efficiencies is found to be ~250-300 mm, which provides the balance between a high pump intensity and a long interaction length extended by filamentation. The maximum efficiencies of TH, FiH, and SVH are measured as ~5×10^{-3}, ~1.5×10^{-4}, and ~5×10^{-6}, respectively. These are the highest reported TH and FiH efficiencies in the odd-harmonic generation in air. Fig. 17(c) shows, as the pump energy ramps up from 0.1 mJ to 1.7 mJ, the efficiency of TH exhibits a dramatic increase with the slope dependence of energy measured as $E_{TH} \sim (E_{pump})^{5.1}$ up to 0.3 mJ, which is attributed mainly to self-focusing. As the pump energy keeps increasing such that the intensity clamping occurs due to the plasma defocusing, TH is slowed down with $E_{TH} \sim (E_{pump})^{3.0}$. For the FiH generation, the efficiency follows the slope of ~ $(E_{pump})^{3.0}$ due to the filament with the clamped intensity.

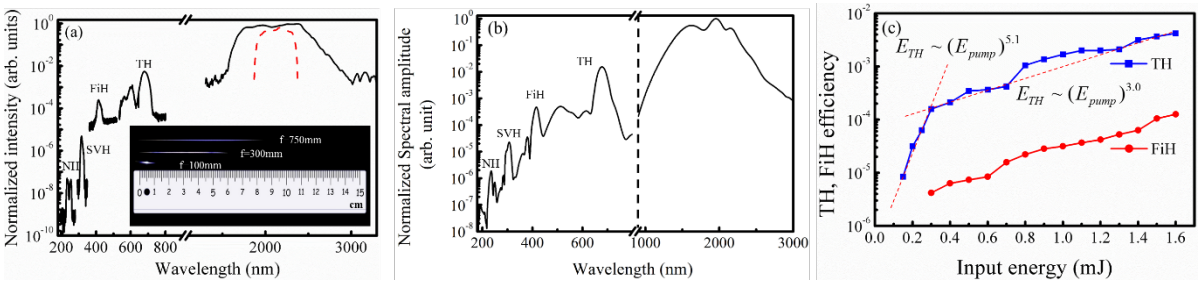

Figure 17: (a) The overall spectrum from the filament. The red dashed curve is the spectrum of the 2.1-μm pump laser. The inset are the filament images focused by lenses with different focal lengths. (b) The simulated harmonics and supercontinuum spectrum with the UPPE model. (c) TH and FiH efficiencies with respect to the pump energy.

The spectral broadening of filaments to the mid-IR is investigated with different focusing geometries. With a tight focus, the spectral broadening primarily towards to a short wavelength side due to a large amount of plasmas created; while with a loose focus, the broadening is dominated by self-phase modulation of neutral atoms which symmetrically extends the spectrum to both sides. With *f*=1000 mm the supercontinuum reaches 3500 nm as shown in Fig. 18(a). The detection of CO_2, the major greenhouse gas, in air is demonstrated using mid-IR filaments via direct absorption spectroscopy [Somekawa10]. The radiation from the mid-IR filament propagates through a 300-mm-long gas cell filled with CO_2 (~340 mbar) for calibration of absorption lines. As shown in Fig. 18(b), two distinct absorption lines of CO_2 at 2690 nm and 2770 nm are clearly recorded. Then, we have measured the mid-IR spectrum from the filament in the ambient air (lab

environment) with different propagation distances. As shown in Fig 18(c), CO_2 fingerprints are present and become outstanding as the propagation distance increasing from 40 cm to 140 cm. This demonstrates that the direct absorption spectroscopy using the kHz, mid-IR filaments provides sufficient sensitivity to detect atmospheric CO_2 which composes only ~400 ppm of air.

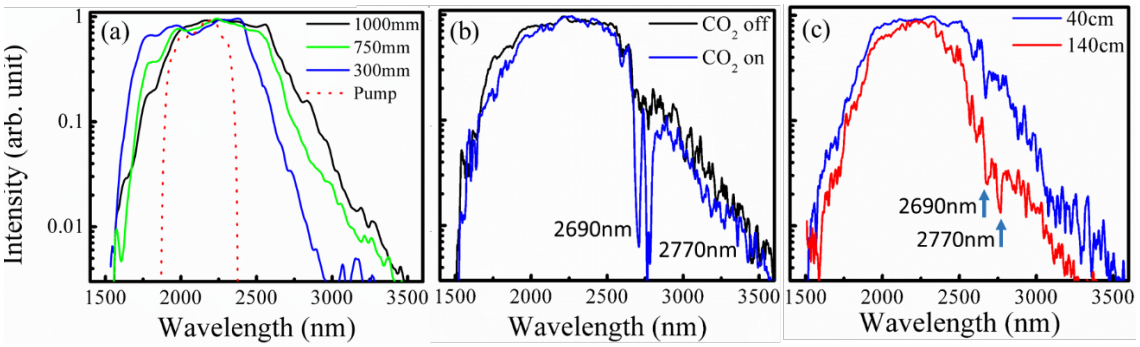

Figure 18: (a) The spectra of the pump pulse and the radiation from the mid-IR filaments generated using a CaF_2 lens with f=1000, 750, and 300 mm. (b) Comparison of the mid-IR spectra from the filament propagating through a CO_2 gas cell with gas being turned on and off. (c) The mid-IR spectra with different propagation distances in air of 40 and 140 cm after the filamentation.

4. Mid-IR sub-cycle pulse synthesis and solid-state HHG

The extension of wavelength coverage into deeper mid-IR beyond ~2 μm brings interesting opportunities for solid-state HHG at moderate energy level (1-30 μJ) as well as gas-phase HHG (mJ level). It also turns out that our multi-mJ, 2.1 μm pulses can efficiently be used for pumping mid-IR OPA covering up to ~10 μm in exotic nonoxide nonlinear crystals, such as $CdSiP_2$ (CSP) and $ZnGeP_2$ (ZGP). Therefore, we took an advantage of our unique capability to develop a novel CEP-stable sub-cycle source in the 2.5–10 μm, mid-IR range and utilized it for studying solid-state HHG in silicon and other materials. In addition, the 2.1 μm pulses was also used to drive intrapulse DFG, for the first time, to directly generate CEP-stable ~8.5 μm pulses.

4.1 Mid-IR sub-cycle pulse synthesis from an OPA covering 2.5-10 μm

In this section, we describe the most recent result on the generation of CEP-stable sub-cycle pulses covering the wavelength range of 2.5–10 μm using this 2.1 μm OPCPA as a pump for CSP or ZGP crystal based mid-IR OPA [Liang17]. Currently, the obtained pulse energy is ~30 μJ at 1 kHz repetition rate which is already high enough to observe strong-field interactions in solids and nano-structures. Figure 19(a) shows the basic concept of the temporal synthesis of two coherent pulses with different colors as well as the actual schematic diagram of an experimental setup for synthesizing mid-IR signal and idler pulses from an OPA.

The key components of this demonstration are as follows:

- **The OPA phase matching bandwidth** of both CSP and ZGP crystals covers the spectral band from 2.5-10 μm when pumped by ~2 μm femtosecond pulses. The bandwidth is broad enough to supports a sub-cycle pulse duration.
- **The collinear type-I OPA** ensures the same polarization and spatial overlap of the signal and idler beams.
- **The thin CSP or ZGP crystal** minimizes temporal walk-off and dispersion to ensure the temporal overlap of signal and idler pulses at different colors.

- **The passively CEP-stable signal and idler pulses** are generated, using a passively CEP-stable pump source, which enables the coherent pulse synthesis of multi-color pulses.

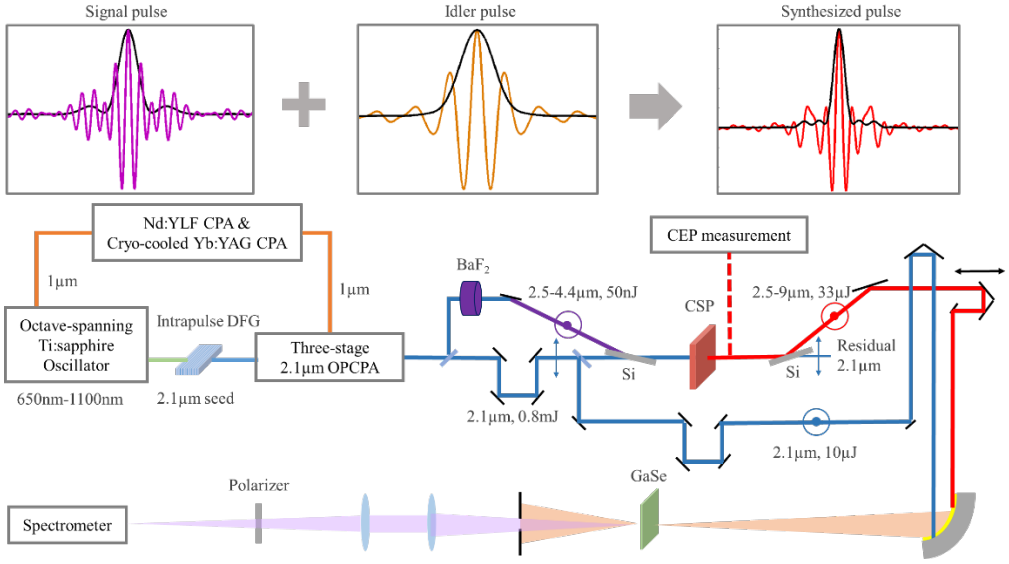

Figure 19: The concept and schematic of the high-energy CEP-stable sub-cycle mid-IR OPA. CPA: chirped-pulse amplifier. Polarizations of the beams are marked by double-headed arrows and concentric circles. 300-μm thick Si wafers at Brewster angle are used as polarization beam splitter and beam combiner to transmit the 2.1-μm pump pulse and reflect the signal and idler pulses. The synthesized pulses and a branch of 2.1-μm reference pulses are sent into XFROG using a 30-μm thick GaSe nonlinear crystal. The synthesis of a sub-cycle mid-IR pulse by coherently combining the sub-2-cycle signal and idler pulses is shown conceptually above the figure.

In the experiment, the multi-mJ CEP-stable, 26 fs, 2.1 μm OPCPA [Hong14] operating at 1 kHz repetition rate serves as the pump of the mid-IR OPA, and a 20 μJ portion of the pump is used for white light generation (WLG) in a BaF_2 plate [Liang15]. The SC extends to 4.4 μm with ~50 nJ pulse energy within the spectral window of 2.5–4.4 μm, serving as the signal for the mid-IR OPA. The signal is combined with the pump in the OPA crystal using an uncoated Si plate at Brewster angle as a polarizing beam splitter (PBS), and another silicon PBS separates the amplified signal and idler pulses from the residual 2.1 μm pump for characterization. A 1.1-mm-thick CSP crystal from BAE Systems with θ=47° is used for type-I parametric conversion.

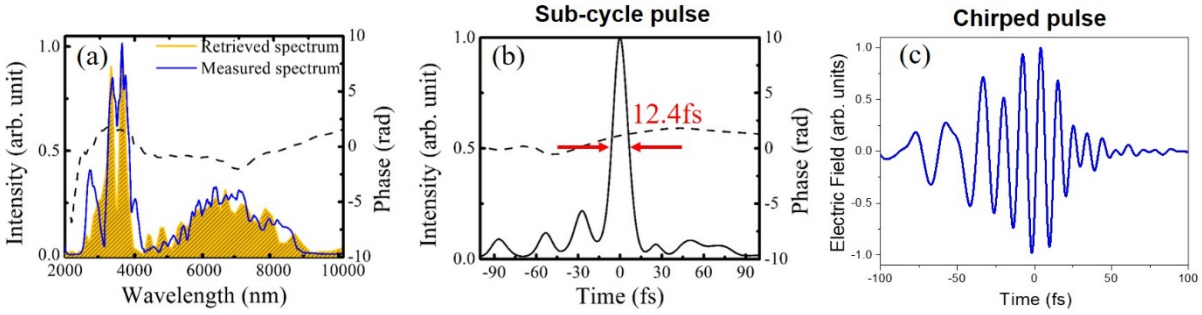

Figure 20: Spectral and temporal characterization of mid-IR sub-cycle and chirped, few-cycle pulses. (a) Measured optical spectrum of amplified signal and idler pulses (solid line) and the retrieved spectrum (shaded) from cross-correlation frequency-resolved optical gating (XFROG) measurements along with the retrived spectral phase (dotted line). (b) The retrieved temporal profile (solid) of the mid-IR 12.4 fs, 0.88-cycle pulses along with the temporal phase (dotted line). (c) The electric field (real part) of a positively chirped, ~43 fs pulse broaded by a 0.5-mm-thick Si filter.

The mid-IR spectra of the amplified signal and idler with 0.8 mJ pump energy are shown in Fig. 20(a), spanning from 2.5 to 9.0 μm. The signal and idler beam profiles, measured with a pyroelectric camera (Spiricon), are near-Gaussian with good spatial overlap. The energy of the signal and idler pulses is ~33 μJ at 0.8 mJ pump energy. The CEP stability of the signal, measured using the self-referencing *f-3f* spectral interferometry (SI), is ~220 mrad rms over 10 minutes. Similarly, the CEP stability of the idler pulse, measured using the cross-reference *f-3f* SI, is ~180 mrad rms over 6 minutes. The temporal walkoff between the signal and idler pulses is estimated as ~5 fs at the CSP crystal. Therefore, in this collinear type-I OPA, the signal and idler pulses are naturally synthesized with <5 fs delay (less than a quarter cycle of the synthesized pulse with a center wavelength of 6 μm).

The temporal profile of the synthesized pule is characterized with a home-built cross-correlation frequency-resolved optical gating (XFROG) apparatus, as depicted in the lower part of Fig. 19. The XFROG signal is detected using an extended InGaAs grating spectrometer (Ocean Optics). In order to preserve the sub-cycle pulse duration of the synthesized pulse, no dispersive optics are used between the OPA and the measurement. The XFROG retrieval in Fig. 20(b) shows that the duration of the synthesized pulse is measured as 12.4 fs in full width and half maximum (FWHM), centered at 4.2 μm, corresponding to 0.88 optical cycle [Liang17]. The retrieved spectrum has a good agreement with the measured spectrum, as found in Fig. 20(a). The pulse energy of 33 μJ and a multi-GW peak power at a kHz repetition rate are already sufficient for studying strong-field interactions in solids and nano-structures [Putnam16]. One important feature of this source is that the idler beam itself provides CEP-stable 1.5-cycle ~10 μJ pulses centered at ~6.5 μm, which is a good standalone source for strong-field experiments as well. Figure 20(c) is the calculated electric-field profile after a 0.5-mm-thick Si filter which was used for solid-state HHG experiments as well. The pulse is positively chirped and elongated to ~43 fs.

4.2 Solid-state HHG in silicon using few-cycle and sub-cycle mid-IR pulses

HHG in solids [Ghimire11, Schubert14, Vampa15] is found to be an excellent tool of studying and controlling the sub-cycle electron dynamics in solid materials. Compared to the near-IR and visible ranges, in the mid-IR ranges the ponderomotive energy of laser pulses is dramatically increased and the Keldysh parameter is much smaller than unity even at relatively modest laser intensities, which enables to study strong-field phenomena in solids without damage. The capability of sub-cycle control of electron currents inside solid materials can open a great opportunity of petahertz or sub-petahertz electronics.

We have used the synthesized mid-IR laser pulses in Figs. 20(b) and (c) to drive HHG in silicon (Si) and other materials, such as MgO, NiO, and diamond. Specifically, we observed the signature of the isolated harmonic emission from solids, for the first time [Liang17]. Here, we describe the main results with Si samples.

A free-standing 200-nm-thick Si (100) sample and a 500-nm-thick Si (100) sample on a 0.5-mm-thick sapphire substrate are used for generating high harmonics. The OPA signal and idler beams with a Gaussian beam diameter of ~5.5 mm are focused using an f=25.4 mm gold-coated off-axis parabolic mirror. The HHG signal is collected using a UV-enhanced aluminum-coated off-axis parabolic mirror and spectrally resolved using a visible-to-UV monochromator with an intensified charge-coupled device. It should be noted that due to the large difference in the centre wavelength between the signal (~3.2 μm) and the idler (~6.4 μm) beams, the focused beam size of the two beams with the same focal length differs by a factor of ~2. Along with the 2 times higher energy

of the signal beam than the idler beam, the HHG is dominated by the signal pulse at the focus (z=0 mm). To observe the clear contribution of the idler pulse, we have acquired most high-harmonic spectra at z=0.5–1.0 mm after the focus where the spot sizes of the signal and idler beams are comparable. The beam size in $1/e^2$ radius at z=0.5 mm is estimated as ~57 μm and ~64 μm for the signal and idler, respectively. The estimated intensity of the ~20 μJ, ~43 fs, chirped pulse with 60 μm of beam waist is ~2×10^{12} W/ cm^2, corresponding to the electric field strength of ~0.4 V/Å. Figs. 21(a) and (b) show the HHG spectra (solid line) with 200-nm and 500-nm-thick Si samples, respectively. Both even and odd harmonics up to the ~19th order of a ~4.4 μm center wavelength are obtained with ~43-fs pulses, whereas odd harmonics (dotted line) are observed with the signal pulses only. The observation of the even harmonics is attributed to the unbalanced electron trajectories and breaks the symmetry in the two-color field [Vampa15]. Fig. 21(c) shows the 4-fold symmetry along the Si <100> axis, confirming that HHG originates from the crystal structure of Si. The strongest harmonics are generated when the laser polarization is parallel to <110> axis. Finally, a near-continuous harmonic spectrum is observed when driven by the sub-cycle pulse with a peak intensity of ~9×10^{12} W/cm^2 corresponding to ~0.8 V/Å of electric field, as shown by Fig. 21(d), which strongly indicates isolated harmonic emission [Liang17]. Further investigations on the CEP dependence along with the pump-probe analysis will enable the observation and control of isolated sub-cycle electron dynamics in solids.

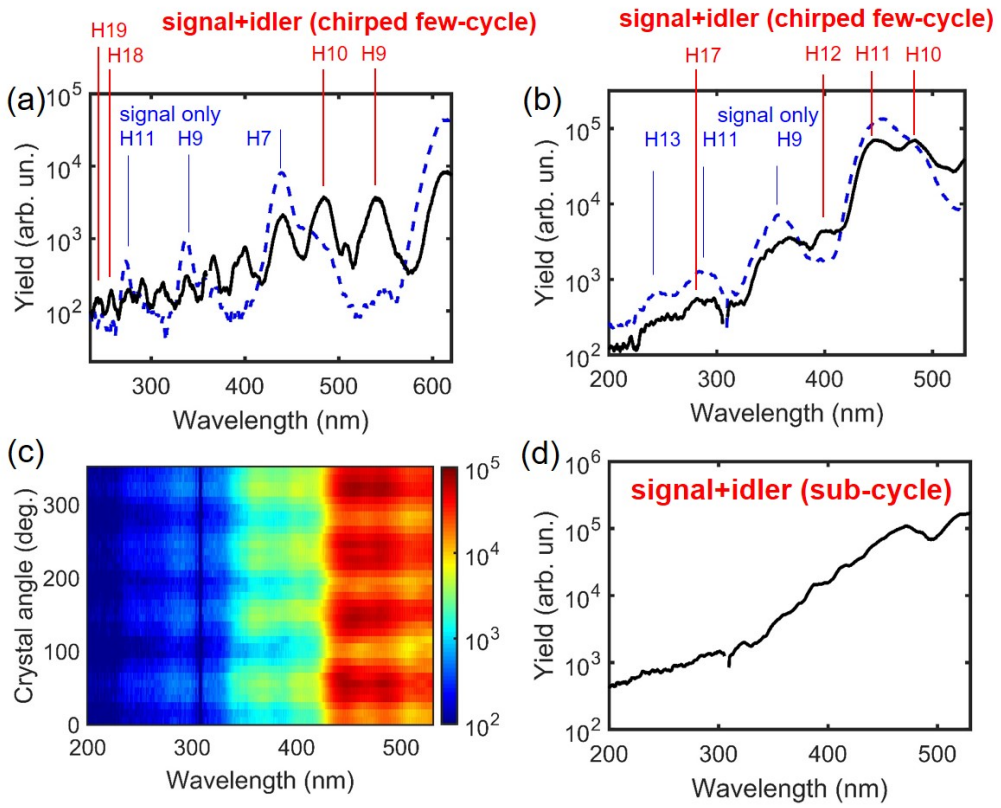

Figure 21: Harmonic spectra generated in a 200-nm-thick free-standing Si sample (a) and a 500-nm-thick Si sample on a 0.5-mm-thick sapphire substrate (b), driven by chirped, ~43 fs, synthesized pulses. The blue dotted line represents the spectrum generated by only the signal pulse. (c) The angle dependence of the harmonic spectra about the Si axis <100> relative to the laser polarization. The harmonics are strongest along <110> axis. (d) The near-continuous harmonic spectrum generated by the synthesized sub-cycle pulse without chirping.

4.3 Intrapulse DFG based femtosecond 8.5 μm source

The intrapulse difference-frequency generation (DFG) pumped by a broadband pulse is a reliable method of producing passively CEP-stable pulses. Mid-IR pulse generation via intrapulse DFG has been demonstrated with near-IR (0.8-1 μm) drive pulses. Since the efficiency and output pulse energy are rather low for intrapulse DFG, these pulses typically seed OPAs for further amplification. If the drive wavelength is shifted to ~2 μm region, the mid-IR intrapulse DFG at >5 μm becomes more efficient due to a lower quantum defect and the excellent phase matching (PM) properties of mid-IR nonlinear crystals based on non-oxide materials that have a relatively low bandgap energy, as proven with the mid-OPA experiment described in Section 4.1. Linear and two-photon absorption with these crystals is significantly reduced for ~2 μm drivers. Moreover, advanced ultrafast lasers at ~2 μm based on Ho-doped crystals [Murari16] and Cr:ZnS/Cr:ZnSe crystals [Mirov15] promises the compact efficient mid-IR conversion with DFG and OPA setups. In this section, we describe the intrapulse DFG in an $AgGaSe_2$ (AGSe) crystal driven by a few-cycle 2.1 μm beam for the generation of CEP-stable femtosecond ~8.5 μm pulses. This is the first demonstration of intrapulse DFG with a ~2 μm beam [Novak18].

We used the 1 kHz, multi-mJ, 26 fs, 2.1 μm OPCPA for driving intrapulse DFG. The driver spectrum spans from 1.85 μm to 2.3 μm (at -10 dB) and the linearly polarized pulse is simply illuminated into a 2-mm-thick type-II AGSe crystal. The neutral density filter attenuates the pulse energy to 250 μJ. A zero-order half-wave plate changes the polarization angle in order to split the driver beam between extraordinary pump and ordinary signal beams at the crystal. The AGSe crystal is placed about 300 mm behind the focus of an f=1000 mm CaF_2 lens in order to keep the driving intensity below the crystal's damage threshold. The estimated peak intensity on the crystal was ~200 GW/cm^2. The type-II interaction in AGSe, with an extraordinary polarization of the idler, has higher effective second-order nonlinear coefficient and more favorable PM for the incident broadband 2.1 μm pulse in comparison to type-I PM. Therefore, the AGSe crystal is cut for Type-II PM with θ = 53.1° and φ = 0°. Such PM enables, e.g., the following interaction, 1.88 μm – 2.28 μm → 10.6 μm, for which the effective second-order nonlinear coefficient, d_{eff} = 33.9 pm/V. We can expect to produce intrapulse DFG pulses ~10 μm wavelength.

The 2.1 μm drive beam is filtered out by a long-pass filter (LPF) with cut-on wavelength of 4.5 μm or 2.4 μm on the way to the diagnostics part of the setup. An off-axis parabola couples the beam into a multimode mid-IR fiber with the transmission range between 3 and 15 μm. The fiber is coupled into a scanning-type grating monochromator with a liquid nitrogen cooled MCT detector. The idler energy is measured behind the LPF using a pyro-electric detector.

The output energy of the DFG idler pulses with the 4.5 μm LPF was optimized by changing the driver polarization by the half-wave plate rotation, which changed the ratio between the extraordinary (pump part) and ordinary (signal part) waves in the crystal (Fig. 22(a)). A maximum idler pulse energy of ~2 μJ (conversion efficiency of 0.8 %) was measured for the beam polarization of ~80° and ~280° relative to the ordinary axis of AGSe, where the most of the drive beam correspond to the extraordinary polarization, indicating that the majority of the driver energy is used for the pump part, resembling the case of OPA with strong pump and weak signal pulses.

The measured idler spectrum (Fig. 22(b)) shows the peak at ~8.5 μm with a bandwidth of ~1.4 μm (FWHM), while it covers ~3.5 μm at -10 dB of width. The mechanism of intrapulse DFG is supported by 3D numerical simulations [Lang13]. Because of the high nonlinear refractive index of AGSe of 350×10^{-16} cm^2/W, we have included SPM and self-focusing into the calculations. The calculated spectrum for PM angle of θ=56.5° (Fig. 22(c)) shows a quantitative agreement with the

measured one. The calculated temporal profile of an output uncompressed idler pulse shown as an inset of Fig. 22(c) has a duration of 80 fs (FWHM), which corresponds to sub-3 optical cycles.

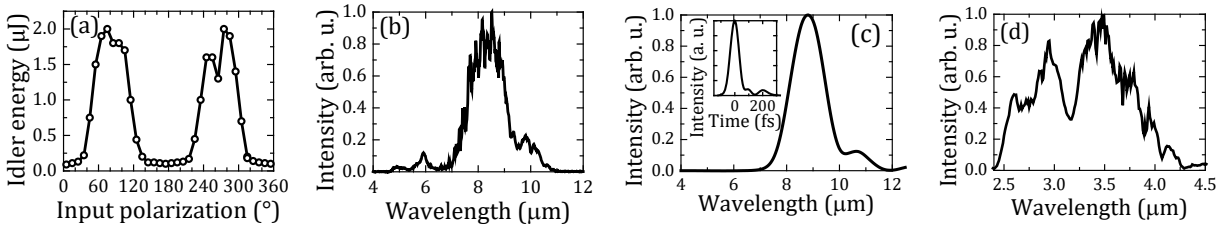

Figure 22: (a) Measured dependence of the output idler pulse energy on the input polarization angle of drive pulse to ordinary axis. (b) Measured spectrum of intrapulse DFG output with a 4.5 μm LPF and (c) calculated idler spectrum. Inset of (c) shows the calculated temporal profile of uncompressed idler pulse. (d) Measured output spectrum in 2.4-4.5 μm corresponding to the signal part of the drive pulse after propagation.

The idler peak at 8.5 μm is blueshifted compared to our original estimation of ~10 μm. According the PM curve for θ=56.5° this peak is generated by pump and signal wavelengths of ~2.0 and ~2.6 μm, respectively. Because the original 2.6 μm content of drive pulse is very small, the spectral broadening and amplification of the signal part of the drive pulse have to take place during the propagation through the crystal. Our simulation confirms that SPM plays an important role here. The spectral broadening is confirmed as well by the measured signal spectrum with a 2.4 μm LPF, shown as Fig. 22(d), which spans up to ~4.3 μm. Although the <2.6 μm part is significantly attenuated by the coupling fiber, the signal content at ~2.6 μm satisfactorily explains the blueshift of the idler wavelength from 10 μm to 8.5 μm.

III. Conclusions

The MIT-KSU "Isolated Attosecond Pulse Generation Using Synthesized Mid-IR Pulses" program enabled not only to develop novel few-cycle and sub-cycle mid-IR laser sources based on OPA, OPCPA, and pulse synthesis but also to study strong-field physics and extreme nonlinear optics driven by mid-IR laser pulses in the wavelength range of 2–10 μm. Specifically, we developed a long-term stable, multi-mJ, kHz, 26 fs, 2.1 μm OPCPA source. Using this unique source, we experimentally demonstrated 1) water-window soft X-ray HHG up to 450 eV, 2) sub-cycle control of soft X-ray yield from two-color (ω+3 ω) driven HHG, 3) mid-IR laser filamentation in solids and ambient air, 4) sub-cycle pulse synthesis from an OPA in the wavelength range of 2.5–10 μm, 5) continuous harmonic spectra from solid-state HHG in silicon as a signature of isolated harmonic emission. Our theoretical studies uncover how to improve the characteristics of high harmonics in different spectral regions from both the single-atom and macroscopic aspects, by optimizing the macroscopic parameters and the multi-color laser waveforms, and by increasing the gas pressure in a high-ionization medium. Under this grant, we believe we have made significant advancement and balanced efforts on novel laser source technology, applications to attosecond science and nonlinear optics, and comprehensive theoretical studies. As evidenced by numerous high-quality publications (18 journal papers) and conference presentations (26 presentations), outcomes under this grant have made a tremendous impact on fundamental and applied sciences within ultrafast laser community, which is strongly aligned with the goal of AFOSR as well as DoD in general.

IV. Publications and Patent applications supported by this project:

Archival publications during entire project period (Sept. 2014 – Nov. 2017):
<Journal paper>

1) Cristian Manzoni, Oliver Mücke, Giovanni Cirmi, Shaobo Fang, Jeffrey Moses, Shu-Wei Huang, Kyung-Han Hong, Giulio Cerullo, Franz X. Kärtner, “Coherent pulse synthesis: towards sub-cycle optical waveforms (invited review),” Laser and Photonics Reviews **9**, 129-171 (2015).
2) Chun-Lin Chang, Peter Krogen, Houkun Liang, Gregory J. Stein, Jeffrey Moses, Chien-Jen Lai, Jonathas P. Siqueira, Lius E. Zapata, Franz X. Kärtner, and Kyung-Han Hong, “Multi-mJ, kHz picosecond deep ultraviolet source,” Opt. Lett. **40**, 665 (2015).
3) Houkun Liang, Peter Krogen, Ross Grynko, Ondrej Novak, Chun-Lin Chang, Gregory J. Stein, Darshana Weerawarne, Bonggu Shim, Franz X. Kärtner, and Kyung-Han Hong, “Three-octave-spanning supercontinuum generation and sub-two-cycle self-compression of mid-infrared filaments in dielectrics,” Opt. Lett. **40**, 106 (2015).
4) Chun-Lin Chang, Peter Krogen, Kyung-Han Hong, Luis E. Zapata, Jeffrey Moses, Anne-Laure Calendron, Houkun Liang, Chien-Jen Lai, Gregory J. Stein, and Franz X. Kärtner," High-energy, kHz, picosecond hybrid Yb-doped chirped-pulse amplifier," Opt. Express **23**, 10132 (2015).
5) Kyung-Han Hong, Chun-Lin Chang, Peter Krogen, Houkun Liang, Gregory J. Stein, Jeffrey Moses, Chien-Jen Lai, and Franz X. Kärtner, “Multi-mJ, kHz picosecond deep UV source based on a frequency-quadrupled cryogenic Yb:YAG laser,” Proc. of SPIE **9513**, High-Power, High-Energy, and High-Intensity Laser Technology II, 95130U (2015).
6) Cheng Jin, Gregory J. Stein, Kyung-Han Hong, and C. D. Lin, “Generation of Bright, Spatially Coherent Soft X-Ray High Harmonics in a Hollow Waveguide Using Two-Color Synthesized Laser Pulses,” Phys. Rev. Lett. **115**, 043901 (2015).
7) Cheng Jin, Kyung-Han Hong, and C. D. Lin, “Optimal generation of high harmonics in the water-window region by synthesizing 800-nm and mid-infrared laser pulses,” Opt. Lett. **40**, 3754 - 3757 (2015).
8) Chien-Jen Lai, Kyung-Han Hong, Jonathas Siqueira, Peter Krogen, Chun-Lin Chang, Gregory J. Stein, Houkun Liang, Phillip D. Keathley, Guillaume Laurent, Jeffrey Moses, Luis E. Zapata, and Franz X. Kärtner, “Mid-infrared kHz OPCPA and Yb-doped pump lasers for strong-field nonlinear optics (invited),” Journal of Optics **17**, 094009 (2015).
9) Houkun Liang, Darshana Weerawarne, Peter Krogen, Rostislav I. Grynko, Chien-Jen Lai, Bonggu Shim, Franz X. Kärtner, and Kyung-Han Hong, “Mid-infrared laser filaments in air at a kilohertz repetition rate,” Optica **3**, 678-681 (2016).
10) Gregory J. Stein., Phillip D. Keathley, Peter Krogen, Houkun Liang, Jonathas P. Siqueira, Chun-Lin Chang, Chien-Jen Lai, Kyung-Han Hong, Guillaume M. Laurent, and Franz X. Kärtner, "Water-window soft X-ray high-harmonic generation up to the nitrogen K-edge driven by a kHz, 2.1 μm OPCPA source," J. Phys. B **49**, 155601 (2016).
11) Cheng Jin, Kyung-Han Hong, and C. D. Lin, “Optimal generation of spatially coherent soft X-ray isolated attosecond pulses in a gas-filled waveguide using two-color synthesized laser pulses,” Sci. Rep. **6**, 38165 (2016).
12) Cheng Jin and C. D. Lin, “Spatially coherent high-order harmonics generated at optimal high gas pressure with high-intensity one- or two-color laser pulses,” Phys. Rev. A **94**, 043804 (2016).
13) Cheng Jin and C. D. Lin, “Optimization of multi-color laser waveform for high-order harmonic generation,” Chin. Phys. B (Review) **25**, 094213 (2016).

14) Anh-Thu Le, Hui Wei, Cheng Jin, and C D Lin, Strong-field approximation and its extension for high-order harmonic generation with mid-infrared lasers, J. Phys. B (Tutorial) **49**, 053001 (2016).
15) Houkun Liang, Peter Krogen, Zhou Wang, Hyunwook Park, Tobias Kroh, Kevin Zawilski, Peter Schunemann, Jeffrey Moses, Louis F. DiMauro, Franz X. Kärtner, and Kyung-Han Hong, "High-energy mid-infrared sub-cycle pulse synthesis from a parametric amplifier," Nature Communications **8**, 141 (2017).
16) Cheng Jin, Kyung-Han Hong, and C. D. Lin, Macroscopic scaling of high-order harmonics generated by two-color optimized waveforms in a hollow waveguide, Phys. Rev. A **96**, 013422 (2017).
17) Hung-Wei Sun, Pei-Chi Huang, Yi-Hsuan Tzeng, Jen-Ting Huang, C. D. Lin, Cheng Jin, and Ming-Chang Chen, Extended phase matching of high harmonic generation by plasma-induced defocusing, Optica **4**, 976-981 (2017).
18) Ondřej Novák, Peter R. Krogen, Tobias Kroh, Tomáš Mocek, Franz X. Kärtner, and Kyung-Han Hong, "Femtosecond 8.5 μm source based on intrapulse difference-frequency generation of 2.1 μm pulses," Optics Letters **43** (6), *in press* (March 2018).

<In preparation >

A.1) Tobias Kroh, Cheng Jin, Peter Krogen, Philip D. Keathley, Anne-Laure Calendron, Jonathas P. Siqueira, Houkun Liang, Edilson L. Falcao-Filho, Chii Dong Lin, Franz X. Kärtner, and Kyung-Han Hong, "Enhanced high-harmonic generation up to the soft X-ray region driven by mid-infrared pulses mixed with their third harmonic," Optics Express, *to be submitted* (March, 2018).

<Conference paper>

1) Houkun Liang, Peter Krogen, Ross Grynko, Ondrej Novak, Chun-Lin Chang, Gregory J. Stein, Darshana Weerawarne, Bonggu Shim, Franz X. Kärtner, and Kyung-Han Hong, "Mid-IR Filamentation in Dielectrics: 3-octave-spanning Supercontinuum Generation and Sub-2-cycle Self-compression," CLEO 2015 (San Jose, CA, May 10-15, 2015), FTu4D.2 oral presentation.
2) Chun-Lin Chang, Peter Krogen, Houkun Liang, Gregory J. Stein, Jeffrey Moses, Chien-Jen Lai, Jonathas P. Siqueira, Luis E. Zapata, Franz X. Kärtner, and Kyung-Han Hong, "Multi-mJ, kHz, intense picosecond deep-ultraviolet source," CLEO 2015 (San Jose, CA, May 10-15, 2015), SF2M.5, oral presentation.
3) Gregory J. Stein, Chien-Jen Lai, Phillip D. Keathley, Peter Krogen, Houkun Liang, Chun-Lin Chang, Kyung-Han Hong, Guillaume M. Laurent, and Franz X. Kärtner, "Versatile simulation package for ultrafast pulse propagation and high harmonic generation," CLEO 2015 (San Jose, CA, May 10-15, 2015), JW2A.36, poster presentation.
4) Kyung-Han Hong, "High-power, ps, kHz Yb-doped CPA systems for ultrafast strong-field nonlinear optics (invited)," Topical meeting on picosecond thin-disk laser technology for EUV sources (April 17, 2015, Prague, Czech).
5) Kyung-Han Hong, Chun-Lin Chang, Peter Krogen, Houkun Liang, Gregory J. Stein, Jeffrey Moses, Chien-Jen Lai, and Franz X. Kärtner, "Multi-mJ, kHz picosecond deep UV source based on a frequency-quadrupled cryogenic Yb:YAG laser (invited)," SPIE Optics + Optoelectronics 2015 (Prague, Czech Republic, April 13-16, 2015), Paper 9513-28.
6) Houkun Liang, Peter Krogen, Ross Grynko, Ondrej Novak, Chun-Lin Chang, Gregory J. Stein, Darshana Weerawarne, Bonggu Shim, Franz X. Kärtner, and Kyung-Han Hong, "3-octave Supercontinuum Generation and Sub-2-cycle Self-compression of Mid-IR Filaments

in Dielectrics," Advanced Solid-State Lasers 2014 (Shanghai, China, Nov. 16-21, 2014), postdeadline paper ATu5A.4.

7) Chun-Lin Chang, Kyung-Han Hong, Peter Krogen, Houkun Liang, Gregory J. Stein, Jeffrey Moses, Chien-Jen Lai, Jonathas P. Siqueira, Luis E. Zapata, and Franz X. Kärtner, "Multi-mJ, kHz intense picosecond deep ultraviolet source based on a frequency-quadrupled cryogenic Yb:YAG laser," Advanced Solid-State Lasers 2014 (Shanghai, China, Nov. 16-21, 2014), oral presentation ATu3A.3.
8) Peter Krogen, Houkun Liang, K. Zawilski, P. Schunemann, T. Lang, U. Morgner, Jeffrey Moses, Franz X. Kärtner, and Kyung-Han Hong, "Octave-spanning 1.5-optical-cycle 6.5-μm OPA pumped by 2.1-μm OPCPA," CLEO 2016 (San Jose, CA, June 6-10, 2016), Stu3I.
9) Houkun Liang, Peter Krogen, Kevin Zawilski, Peter Schunemann, Franz X. Kärtner, and Kyung-Han Hong, "Phase-stable sub-single-cycle pulses from parametric amplification covering the entire range of 2.5-10 μm," OSA Congress on High-Brightness Sources 2016 (Long Beach, CA, Mar. 20-22, 2016), MICS/HILAS postdeadline paper JT3A.3.D.
10) Houkun Liang, Peter Krogen, K. Zawilski, P. Schunemann, T. Lang, U. Morgner, Franz X. Kärtner, Jeffrey Moses, and Kyung-Han Hong, "Octave-spanning 6-μm OPA pumped by 2.1-μm OPCPA (invited)," OSA Congress on High-Brightness Sources 2016 (Long Beach, CA, Mar. 20-22, 2016), MICS, paper MS4C.1.
11) Houkun Liang, Peter Krogen, Darshana Weerawarne, Chien-Jen Lai, Rostislav Grynko, Bonggu Shim, Franz X. Kärtner, and Kyung-Han Hong, "Mid-IR laser filamentation in air at a kHz repetition rate," OSA Congress on High-Brightness Sources 2016 (Long Beach, CA, Mar. 20-22, 2016), MICS, paper MT2C.5.
12) Phillip D. Keathley, Gregory J. Stein, Peter Krogen, Houkun Liang, Jonathas P. Siqueira, Chun-Lin Chang, Chien-Jen Lai, Kyung-Han Hong, Guillaume M. Laurent, and Franz X. Kärtner, "Water-window soft X-ray high-harmonic generation up to the nitrogen K-edge driven by a kHz, 2.1 μm OPCPA source," OSA Congress on High-Brightness Sources 2016 (Long Beach, CA, Mar. 20-22, 2016), Compact X-ray Sources, paper ET5A.3.
13) Kyung-Han Hong, "Extreme nonlinear optics in the strong mid-IR fields (invited)," High-Power Laser Science and Engineering 2016 (Shanghai, China, Mar. 16-18, 2016).
14) Kyung-Han Hong, "Ultrafast nonlinear optics in the extreme (invited)," X Symposium of Lasers and its Applications (Sept. 22-25, 2015, Recife, Brazil).
15) Cheng Jin, Gregory J. Stein, Kyung-Han Hong, and C. D. Lin, "Efficient generation of low divergent soft X-ray high harmonics in a hollow waveguide using two-color optimized laser pulses," ATTO2015 (Quebec, Canada, July 6-10, 2015), paper #46 oral presentation.
16) Peter Krogen, Houkun Liang, Kevin Zawilski, Peter Schunemann, Kyung-Han Hong, and Franz X. Kärtner, "Phase-stable mid-infrared sub-single-cycle pulses from OPA covering 2.5-9.0 micron range," Gordon Research Conference on Multiphoton Process (Proctor Academy, Andover, NH, June 19-24, 2016), poster 41.
17) Houkun Liang, Peter Krogen, Darshana Weerawarne, Chien-Jen Lai, Rostislav Grynko, Bonggu Shim, Franz X. Kärtner, and Kyung-Han Hong, "Mid-IR laser filaments in air at a kHz repetition rate," COFIL 2016 (6th international symposium on filamentation) (Quebec City, Canada, Sept. 5-9, 2016), Monday talk.
18) Peter Krogen, Houkun Liang, Kevin Zawilski, Peter Schunemann, Kyung-Han Hong, and Franz X. Kärtner, "Mid-infrared sub-single-cycle pulse synthesis from a parametric amplifier covering the wavelength of 2.5-9.0 μm," ASSL 2016 (Boston, Oct. 31-Nov. 3, 2016), paper AW4A.7.
19) Rostislav I. Grynko, Darshana L. Weerawarne, Xiaohui Gao, Houkun Liang, Henry J. Meyer, Kyung-Han Hong, Alexander L. Gaeta, and Bonggu Shim, "Multi-filament Inhibition

and Resulting Solitary Wave Formation in Condensed Matter," Frontiers in Optics/ Laser Science (FiO/LS) 2016 (Rochester, NY, Oct. 16-21, 2016), postdeadline paper FF2C.1.

20) A.-L. Calendron, J. P. Siqueira, C. Jin, P. R. Krogen, T. Kroh, P. D. Keathley, H. Liang, E. L. Falcão-Filho, C. D. Lin, K.-H. Hong, and F. X. Kärtner, "Enhanced soft X-ray high-harmonic generation driven by two-color (ω+3ω) mid-IR laser pulses," CLEO 2017 (San Jose, CA, May 14-19, 2017), poster JTh2A.50.
21) Ondřej Novák, Peter R. Krogen, Tobias Kroh, Tomáš Mocek, Franz X. Kärtner, and Kyung-Han Hong*, "A CEP-stable, femtosecond 8.5 μm source based on intrapulse DFG of 2.1 μm pulses," CLEO Europe 2017 (Munich, Germany, June 25-29, 2017) CF-7.2.
22) Kyung-Han Hong, Zhou Wang, Tobias Kroh, Hyunwook Park, Peter Krogen, Houkun Liang, Phillip D. Keathley, Louis F. DiMauro, and Franz X. Kärtner, "High-harmonic generation in solids driven by mid-infrared sub-cycle pulses," ATTO 2017 (Xi'an, China, July 2-7, 2017) Thursday morning oral presentation.
23) T. Kroh, C. Jin, P. Krogen, A.-L. Calendron, P. D. Keathley, J. P. Siqueira, H. Liang, E. L. Falcão-Filho, C. D. Lin, F. X. Kärtner and K.-H. Hong*, "Enhanced soft-X-ray high-harmonic generation driven by mid-IR pulses mixed with their third harmonic," ATTO 2017 (Xi'an, China, July 2-7, 2017), poster presentation.
24) K.-H. Hong, P. Krogen, T. Kroh, F. X. Kärtner, and H. Liang, "High-energy mid-infrared sub-cycle pulse synthesis (invited)," CLEO Pacific Rim 2017 (July 30-Aug. 4, 2017), 2-2F-1.
25) Kyung-Han Hong, Zhou Wang, Tobias Kroh, Hyunwook Park, Peter Krogen, Houkun Liang, Louis F. DiMauro, and Franz X. Kärtner, "High-harmonic generation in solids using a mid-infrared sub-cycle pulse synthesizer," FiO/LS 2017 (Washington, DC, Sept. 17-21, 2017) oral presentation LTu4F.2.
26) Kyung-Han Hong, "Extreme nonlinear optics using strong mid-infrared laser pulses (invited)," IEEE Photonics Conference 2017 (Orlando, FL, USA, Oct. 1-5, 2017), TuH1.4.

- Patent

N/A

References

[Chang15] Chun-Lin Chang, Peter Krogen, Kyung-Han Hong, Luis E. Zapata, Jeffrey Moses, Anne-Laure Calendron, Houkun Liang, Chien-Jen Lai, Gregory J. Stein, and Franz X. Kärtner," High-energy, kHz, picosecond hybrid Yb-doped chirped-pulse amplifier," Opt. Express **23**, 10132 (2015).

[Chen10] M. C. Chen, P. Arpin, T. Popmintchev, M. Gerrity, B. Zhang, M. Seaberg, D. Popmintchev, M. M. Murnane, and H. C. Kapteyn, "Bright, coherent, ultrafast soft X-ray harmonics spanning the water window from a tabletop light source," Phys. Rev. Lett. **105**, 173901 (2010).

[Cousin14] S. L. Cousin, F. Silva, S. Teichmann, M. Hemmer, B. Buades, and J. Biegert, "High-flux table-top soft x-ray source driven by sub-2-cycle, CEP stable, 1.85-μm 1-kHz pulses for carbon K-edge spectroscopy," Opt. Lett. **39** 5383–6 (2014).

[Ghimire11] S. Ghimire, A. DiChiara, E. Sistrunk, P. Agostini, L. DiMauro, and D. Reis, "Observation of high-order harmonic generation in a bulk crystal," Nat. Phys. **7**, 138 (2011).

[Henke93] B. L. Henke, E. M. Gullikson, and J. C. Davis, "X-ray interactions: Photoabsorption, scattering, transmission, and reflection at E = 50-30,000 eV, Z = 1-92," Atomic Data and Nuclear Data Tables **54** (2): 181 – 342 (1993).

[Hong10] Kyung-Han Hong, Juliet Gopinath, Darren Rand, Aleem Siddiqui, Shu-Wei Huang, Enbang Li, Benjamin Eggleton, John Hybl, Tso Yee Fan, and Franz X. Kärtner, "High-energy, kHz-repetition-rate, ps cryogenic Yb:YAG chirped-pulse amplifier," Opt. Lett. **35**, 1752-1754 (2010).

[Hong11] Kyung-Han Hong, Shu-Wei Huang, Jeffrey Moses, Xing Fu, Chien-Jen Lai, Giovanni Cirmi, Alexander Sell, Eduardo Granados, Phillip Keathley, and Franz X. Kärtner, "High-energy, phase-stable, ultrabroadband kHz OPCPA at 2.1 μm pumped by a picosecond cryogenic Yb:YAG laser," Opt. Express **19**, 15538-15548 (2011).

[Hong14] Kyung-Han Hong, Chien-Jen Lai, Jonathas Siqueira, Peter Krogen, Jeffrey Moses, Chun-Lin Chang, Gregory J. Stein, Luis E. Zapata, and Franz X. Kärtner, "Multi-mJ, kHz, 2.1-μm optical parametric chirped pulse amplifier and high-flux soft X-ray high-harmonic generation," Opt. Lett. **39**, 3145-3148 (2014).

[Huang11] Shu-Wei Huang, Giovanni Cirmi, Jeffrey Moses, Kyung-Han Hong, Siddharth Bhardwaj, Jonathan R. Birge, Li-Jin Chen, Enbang Li, Benjamin Eggleton, Giulio Cerullo, and Franz X. Kärtner, "High-energy pulse synthesis with sub-cycle waveform control for strong-field physics," Nature Photonics **5**, 475-479 (2011).

[Jin14] C. Jin, G. Wang, H. Wei, A.-T. Le, and C. D. Lin, "Waveforms for optimal sub-keV high-order harmonics with synthesized two- or three-colour laser fields." Nature Communications **5**, 4003 (2014).

[Jin15OL] Cheng Jin, Kyung-Han Hong, and C. D. Lin, "Optimal generation of high harmonics in the water-window region by synthesizing 800-nm and mid-infrared laser pulses," Opt. Lett. **40**, 3754 - 3757 (2015).

[Jin15PRL] Cheng Jin, Gregory J. Stein, Kyung-Han Hong, and C. D. Lin, "Generation of Bright, Spatially Coherent Soft X-Ray High Harmonics in a Hollow Waveguide Using Two-Color Synthesized Laser Pulses," Phys. Rev. Lett. **115**, 043901 (2015).

[Jin16PRA] Cheng Jin and C. D. Lin, "Spatially coherent high-order harmonics generated at optimal high gas pressure with high-intensity one- or two-color laser pulses," Phys. Rev. A **94**, 043804 (2016).

[Jin16SR] Cheng Jin, Kyung-Han Hong, and C. D. Lin, "Optimal generation of spatially coherent soft X-ray isolated attosecond pulses in a gas-filled waveguide using two-color synthesized laser pulses," Sci. Rep. **6**, 38165 (2016).

[Jin17PRA] Cheng Jin, Kyung-Han Hong, and C. D. Lin, "Macroscopic scaling of high-order harmonics generated by two-color optimized waveforms in a hollow waveguide," Phys. Rev. A **96**, 013422 (2017).

[Kroh16] T. Kroh, C. Jin, P. Krogen, A.-L. Calendron, P. D. Keathley, J. P. Siqueira, H. Liang, E. L. Falcão-Filho, C. D. Lin, F. X. Kärtner and K.-H. Hong, "Enhanced soft-X-ray high-harmonic

generation driven by mid-IR pulses mixed with their third harmonic," ATTO 2017 (Xi'an, China, July 2-7, 2017), poster presentation.

[Lang13] T. Lang, A. Harth, J. Matyschok, T. Binhammer, M. Schultze, and U. Morgner, "Impact of temporal, spatial and cascaded effects on the pulse formation in ultra-broadband parametric amplifiers," Opt. Express **21**, 949 (2013).

[Liang15] Houkun Liang, Peter Krogen, Ross Grynko, Ondrej Novak, Chun-Lin Chang, Gregory J. Stein, Darshana Weerawarne, Bonggu Shim, Franz X. Kärtner, and Kyung-Han Hong, "Three-octave-spanning supercontinuum generation and sub-two-cycle self-compression of mid-infrared filaments in dielectrics," Opt. Lett. **40**, 106 (2015).

[Liang16] Houkun Liang, Darshana Weerawarne, Peter Krogen, Rostislav Grynko, Chien-Jen Lai, Bonggu Shim, Franz X. Kärtner, and Kyung-Han Hong, "Mid-infrared laser filaments in air at a kilohertz repetition rate," Optica **3**, 678-681 (2016).

[Liang17] Houkun Liang, Peter Krogen, Zhou Wang, Hyunwook Park, Tobias Kroh, Kevin Zawilski, Peter Schunemann, Jeffrey Moses, Louis F. DiMauro, Franz X. Kärtner, and Kyung-Han Hong*, "High-energy mid-infrared sub-cycle pulse synthesis from a parametric amplifier," Nature Communications **8**, 141 (2017).

[Mirov15] S. B. Mirov, V. V. Fedorov, D. Martyshkin, I. S. Moskalev, M. Mirov, and S. Vasilyev, "Progress in mid-IR lasers based on Cr and Fe-doped II-VI chalcogenides," IEEE J. Sel. Top. Quantum Electron. **21**, 292 (2015).

[Mitrofanov15] A. V. Mitrofanov, A. A. Voronin, D. A. Sidorov-Biryukov, A. Pugzlys, E. A. Stepanov,G. Andriukaitis, T. Flory, S. Alisauskas, A. B. Fedotov, A. Baltuska, and A. M. Zheltikov, "Mid-infrared laser filaments in the atmosphere," Sci. Rep. **5**, 8368 (2015).

[Murari16] K. Murari, G. J. Stein, H. Cankaya, B. Debord, F. Gérôme, G. Cirmi, O. D. Mücke, P. Li, A. Ruehl, I. Hartl, K.-H. Hong, F. Benabid, and F. X. Kärtner, "Kagome-fiber-based pulse compression of mid-infrared picosecond pulses from a Ho:YLF amplifier," Optica **3**, 816 (2016).

[Novak18] Ondřej Novák, Peter R. Krogen, Tobias Kroh, Tomáš Mocek, Franz X. Kärtner, and Kyung-Han Hong, "Femtosecond 8.5 μm source based on intrapulse difference-frequency generation of 2.1 μm pulses," Optics Letters **43** (6), *in press* (2018).

[Popmintchev11] T. Popmintchev, M.-C. Chen, D. Popmintchev, P. Arpin, S. Brown, S. Ališauskas, G. Andriukaitis, T. Balčiunas, O. D. Mücke, A. Pugzlys, A. Baltuška, B. Shim, S. E. Schrauth, A. Gaeta, C. Hernández-García, L. Plaja, A. Becker, A. Jaron-Becker, M. M. Murnane, and H. C. Kapteyn, Bright coherent ultrahigh harmonics in the keV x-ray regime from mid-infrared femtosecond lasers," Science **336**, 1287 (2012).

[Putnam16] W. Putnam, R. Hobbs, P. Keathley, K. Berggren, and F. X. Kärtner, "Optical-field-controlled photoemission from plasmonic nanoparticles," Nat. Phys. **13**, 335 (2017).

[Schubert14] O. Schubert et al., "Sub-cycle control of terahertz high-harmonic generation by dynamical Bloch oscillations," Nature Photon. **8**, 119 (2014).

[Somekawa10] T. Somekawa, M. Fujita, and Y. Izawa, "Direct Absorption Spectroscopy of CO_2 Using a Coherent White Light Continuum," App. Phys. Express **3**, 082401 (2010).

[Stein16] G. J. Stein, P. D. Keathley, P. Krogen, H. Liang, J. P. Siqueira, C.-L. Chang, C.-J. Lai, K.-H. Hong, G. M. Laurent, and F. X. Kärtner, "Water-window soft X-ray high-harmonic generation up to nitrogen K-edge driven by a kHz, 2.1 μm OPCPA source," J. Phys. B **49**, 155601 (2016).

[Takahashi08] E. J. Takahashi, T. Kanai, K. L. Ishikawa, Y. Nabekawa, and K. Midorikawa, "Coherent water window x ray by phase-matched high-order harmonic generation in neutral media," Phys. Rev. Lett. **101**, 253901 (2008).

[Vampa15] G. Vampa, T. J. Hammond, N. Thire, B. E. Schmidt, F. Legare, C. R. McDonald, T. Brabec, and P. B. Corkum, "Linking high harmonics from gases and solids," Nature **522**, 462 (2015).